Article:

Silva, D, Piazolo, S orcid.org/0000-0001-7723-8170 and Daczko, NR (2022) Trapped K-feldspar phenocrysts as a signature of melt migration pathways within active high-strain zones. Journal of Metamorphic Geology. ISSN 0263-4929

https://doi.org/10.1111/jmg.12698

Trapped K-feldspar phenocrysts as a signature of melt migration pathways within active high-strain zones

David Silva[a,b], Sandra Piazolo[a,c], Nathan R. Daczko[a]

[a] ARC Centre of Excellence for Core to Crust Fluid Systems and GEMOC, School of Natural Sciences, Macquarie University, NSW 2109, Australia

[b] Department of Earth, Ocean and Atmospheric Sciences, University of British Columbia, Vancouver, BC V6T 1Z4, Canada

[c] School of Earth and Environment, Institute of Geophysics and Tectonics, University of Leeds, Leeds, LS2 9JT, United Kingdom

Corresponding author: David Silva (david.barbosa-da-silva@students.mq.edu.au)

Keywords: High-strain zone; Metasomatism; Melt extraction; Collapse structures; Phenocrysts.

ABSTRACT

Melt migration through high-strain zones in the crust fundamentally influences their rheological behaviour and is important for the transfer of fluids to upper crustal regions. The inference of former melt-present deformation, based on field observations, may be hampered if the high-strain zone experience a low time-integrated melt flux or high melt volume expulsion during deformation. In these cases, typical macro-scale field evidence of former melt presence limits interpretations. In this contribution, we investigate igneous field evidence ranging from obvious to cryptic in the Gough Dam shear zone (central Australia), a 2–4 km wide high-strain zone shown to have acted as a significant melt pathway during the Alice Springs Orogeny. Within bands of the high-strain zone, granitic lenses are easily discernible in the field and are inferred to have formed during melt present

deformation. Related coarse K-feldspar is observed in biotite-rich (> 75 vol%) schist (glimmerite) as either isolated grains, forming trails (sub)parallel to the main foliation, or in aggregates with subordinate quartz. Detailed characterisation of the granitic lenses shows that pockets of phenocrysts may be entrained in the shear zone. If melt expulsion and melt-rock interaction is severe, isolated K-feldspar grains in glimmerite may form. These grains exhibit (i) partially preserved crystal faces; (ii) a lack of internal grain deformation; (iii) reaction textures preferentially formed along the main crystallographic axes showing dissolution of K-feldspar and precipitation of dominantly biotite; (iv) low-strain domains between multiple K-feldspar grains are inferred to enclose crystallised melt pockets, with some apparently isolated grains showing connectivity in three dimensions; and (v) a weak quartz and K-feldspar crystallographic preferred orientation. These observations suggest an igneous phenocrystic origin for the isolated K-feldspar grains hosted in glimmerite which is consistent with the observed REE concentration patterns with positive Eu anomaly. We propose that the K-feldspar phenocrysts are early-formed crystals that were entrained into the glimmerite rocks as reactive melt migrated through the actively deformating high-strain zone. Previously entrained K-feldspar phenocrysts were trapped during the collapse of the melt pathway when melt flux-related fluid pressure waned while confining pressure and tectonic stress were still significant. The active deformation facilitated expulsion or loss of the melt phase but retainment and trapping of phenocrysts. Hence, the presence of isolated or “trains” of K-feldspar phenocrysts are a cryptic signature of syndeformational melt transfer. If melt transfer occurs in an open chemical system, phenocrysts will be entrained within the reaction product of melt rock interaction. We suggest that these so-called “trapped phenocrysts” are a viable indicator of former syntectonic melt passage through rocks.

1. INTRODUCTION

High-strain zones are important crustal-scale conduits for melt transfer from regions of melt production (lower- to middle-crust) to shallower crustal depths, significantly contributing to the observed segregation of highly silicic melt towards the upper crust (Hollister & Crawford, 1986;

Hutton, 1988; D'lemos *et al.,* 1992; Brown, 1994; Vigneresse, 1995; Weinberg *et al.,* 2004; Brown & Rushmer, 2006; Etheridge *et al.*, 2020). Furthermore, the former presence of melt in highly strained rocks suggests a high-strain zone with very weak rheology, and by consequence increased strain localisation in such zones compared to the surrounding consolidated rocks (Rosenberg & Handy, 2005; Levine *et al.,* 2013; Searle, 2013; Lee *et al.,* 2018; Daczko & Piazolo, 2022). Whilst melt-present high-strain zones preserve signatures of the former presence of melt (e.g., granitic lenses), not all melt-present high-strain zones may show such clear signatures of former magmatic activity. The recognition of such zones is difficult if they preserve low crystallised melt volumes due to limited presence of macroscopic crystallised igneous material (i.e., leucosome) arranged in seams, pockets or dykes in the deformed rock (e.g., Weinberg *et al.,* 2013; Stuart *et al.,* 2017, 2018; Daczko & Piazolo, 2022). However, low percentages of preserved crystallised melt volume are expected if deformation is synchronous with melt presence, as deformation will markedly enhance movement of melt (Van der Molen & Paterson, 1979; Rosenberg & Handy, 2005; Brown & Solar, 1998; Collins & Sawyer, 1996; Etheridge *et al.*, 2020). Therefore, the signature of the former presence of melt in high-strain zones may be cryptic at the outcrop scale and requires in-depth microstructural analysis to identify it (Daczko & Piazolo, 2022). For example, microstructures may include small mono- or multiphase pockets at triple points and/or elongated interstitial grains (Beere, 1975; Von Bargen & Waff, 1986; Holness & Sawyer, 2008; Závada *et al.,* 2007; Stuart *et al.,* 2017, 2018; Lee *et al.,* 2018). In addition, if the melt was chemically reactive at the time of deformation, a change in mineral assemblage and bulk composition of the zone also occurs (e.g., Daczko *et al*., 2016; Stuart *et al*., 2018; Meek *et al*., 2019; Piazolo *et al*., 2020). If melt fractions where locally high (>> 10 vol%), areas that were occupied by melt before expulsion, develop so-called "collapse structures" which are most easily recognised if the channelised melt network was at a high angle to the general rock foliation (e.g., Bons, 1999; Marchildon & Brown, 2003; Druguet & Carreras, 2006; Diener *et al*., 2014; Wolfram *et al*., 2017).

In summary, it is difficult to recognise in the field the former presence of melt in highly strained rocks if deformation was synchronous with melt presence. However, failure to recognise former melt presence, may lead to erroneous interpretations of high-strain rocks in terms of their rheology at the time of deformation, based on the difficulty of quantifying the former melt volume fraction, along with inaccurate interpretations of the strain history and even incorrect identification of the rock type (Bons, 1999; Kriegsman, 2001; Brown, 2005; Bons *et al.,* 2008, 2009). Thus, the recognition of potentially cryptic signatures of the former presence of melt in high-strain rocks is crucial to interpret and understand melt migration through the lithosphere, as well as to develop a thorough understanding of the tectonic and magmatic history of an area, including periods of significant melt transfer.

To establish what field signatures can be used to recognise former syntectonic melt presence, it is necessary to develop an understanding of how igneous components may be preserved despite syntectonic melt flux and expulsion. In this contribution, we present a detailed microstructural study of rocks present in the 2–4 km-wide Gough Dam shear zone that was active during the Alice Springs Orogeny (ASO) in central Australia, which has been shown to have deformed in the presence of melt (Piazolo *et al.,* 2020; Silva *et al.,* 2022). This high-strain zone is characterised by highly strained, biotite-dominated schist (glimmerite schist) formed by melt-mediated metasomatic reaction with a granulite precursor rock (Silva *et al.,* 2022). To advance our ability to recognise formerly melt-present high-strain zones, we investigate the microstructural signature of samples with obvious igneous components and samples lacking these clear field signatures. Chosen samples span from granitic lenses to isolated grains or trains of mm-scale faceted K-feldspar immersed in the glimmerite *sensu stricto* (*s.s.*). Granitic lenses occur with or without selvedges and are inferred from previous studies to represent lenses of magma frozen in the high-strain zone (Piazolo *et al*., 2020).

Here, we use quantitative orientation mapping, scanning electron microscope (SEM) based imaging and chemical analysis to characterise quartz and K-feldspar microstructures. Results show that for both granitic lenses and glimmerite samples, the microstructural characteristics are not typical for high-strain rocks deformed by solid-state deformation dominated by dislocation creep. The solid igneous minerals such as coarse, K-feldspar grains remain largely undeformed, as the present melt accommodates most strain and effectively "shields" the solid grains. Based on our results, we suggest that K-feldspar phenocrysts within a product of melt-rock interaction, e.g., a glimmerite schist, may be used as an additional indicator for the recognition of former melt flux in high-strain zones. We interpret their presence in highly metasomatised rocks as a consequence of early feldspar crystallisation in a syntectonic melt, succeeded by the structural collapse of the adjacent rocks during melt expulsion, resulting in K-feldspar entrapment in the biotite dominated schist. As such "trapped phenocrysts" may be used to delineate former pathways of melt migrating through high-strain zones from deeper crustal origins.

2. GENERAL GEOLOGICAL BACKGROUND

The study area is in the Arunta Region, central Australia, which was most recently deformed in the ASO, a ~700 km long by ~80 km wide intracontinental orogeny that spanned the period of 450 to 300 Ma (Collins & Teyssier, 1989; Hand & Sandiford, 1999; Mawby *et al.,* 1999; Scrimgeour, 2013; Fig. 1). An extensive regional system of anastomosing high-strain zones and localised deep crustal thrust faults are present, and these cuts most of the high-grade metamorphic complexes in the region, with peak *P-T* conditions of 5.0–6.5 kbar and 500°–600° C in the west and central parts of the orogen (Cartwright *et al.,* 1999; Ballèvre *et al.,* 2000; Raimondo *et al.,* 2011, 2014; Fig. 1). Crustal thickening with an estimated ~100 km of horizontal shortening occurred during tectonic N-S compression and involved the exhumation of granulitic basement rocks (Shaw *et al.,* 1984; Teyssier, 1985; Collins & Teyssier, 1989). Crustal shortening during the ASO induced intense and large-scale crustal denudation of metamorphic and igneous terranes, with deposition of multiple synorogenic sedimentary sequences up to 4km in thickness in basins surrounding the Arunta Region (Haines *et al.*, 2001; Raimondo *et al.,* 2014). Multiple episodes of pegmatite intrusions in the Arunta Region took place throughout the duration of the ASO and their ages correlate with the temporal formation of regional structures and deposition of synorogenic sedimentary sequences in the adjacent basins (Buick *et al.,* 2008; Varga *et al.,* 2022). The lack of ASO-aged partial melting of the basement rocks suggests a deep-seated parental melt source for the exposed ASO-aged igneous rocks, which comprise mainly pegmatite dykes and minor granite plutons (Buick *et al.,* 2008; Piazolo *et al.,* 2020). Tectonic compression was enhanced during periods of extension in the Tasmanides Orogeny, adjacent to the Eastern Australian plate boundary (Raimondo *et al.,* 2014; Silva *et al.,* 2018). The study area lies in the Strangways Metamorphic Complex (SMC) formed during the Strangways Event (*c*. 1735–1690 Ma; Fig. 1). The SMC is cut by steeply dipping, km-wide, hydrous and multi-reactivated high-strain zones that were formed during the ASO (Fig. 1). These comprise upper amphibolite- to greenschist-facies schist belts that include layers of K-feldspar-biotite-quartz schist (i.e., 40–60 vol% mica; identified hereafter as glimmerite schist) and glimmerite *sensu stricto* (*s.s*) (i.e., > 75 vol% mica with very low proportions of quartz).

Granitic lenses with and without glimmerite selvedges and glimmerite schist were sampled from the Gough Dam shear zone (GDSZ), a E-W to NNW-SSE trending, 2–4 km-wide, steeply dipping (60°–90° towards N) high-strain zone (Fig. 1). Based on shear band orientations and sigma clast kinematic indicators, the GDSZ represents a S-directed reverse high-strain zone that juxtaposed the northern SMC with the Harts Range Metamorphic Complex (HRMC) (Collins & Shaw, 1995; Bendall, 2000; Fig. 1). This high-strain zone is characterised by metasomatic hydration of the bi-modal interlayered anhydrous mafic-felsic granulites, quartzo-feldspathic gneisses, minor calcsilicate and amphibolite rocks constituting the Palaeoproterozoic SMC basement of the Arunta Region (Piazolo *et al.,* 2020; Silva *et al.,* 2022). The formation of glimmerite schist in the GDSZ and glimmerite selvedges observed around granitic lenses was recently proposed by Silva *et al.* (2022) as involving multiple periods of migration of extensive volumes of hydrous peraluminous melt through the high-strain zone during the ASO. Reaction of the migrating melts with the precursor quartzo-feldspathic granulite rocks was inferred within mainly channelised pathways parallel to the high-strain zone foliation. The magnitude of melt needed to drive the melt-mediated reaction forming glimmerite and the size and longitudinal continuity of field indicators of former melt flux increases towards the centre of the GDSZ (Silva *et al.*, 2022). Recent research on the nearby Cattle Water Pass shear zone also demonstrated that melt-rock interaction and migration of significant volumes of melt through high-strain zones was important in enriching the rocks in oxide minerals such as ilmenite (Ghatak *et al.*, 2022).

2.1. Field relationships

The main rock types present in the GDSZ schist belt are phyllonitic biotite-rich quartzo-feldspathic gneiss (hereafter named granitic gneiss), felsic and mafic granulite pods, quartz-rich rafts, and sparse cm-wide garnet-bearing granulites; the high-strain rocks contain biotite, sillimanite, and rare kyanite, delineating the steep north-plunging lineation (Ballèvre *et al.,* 1997). Continuous cm- to dm-scale banding parallel to the GDSZ foliation is observed in the study area and these span compositions ranging from granitic (i.e., near-euhedral Kfs ± qz and subordinate plagioclase and biotite (< 5 vol%); Fig. 2a) to glimmerite bands of high biotite content (up to 80 vol%; Fig. 2b). Small lenses of variably deformed granite resembling pinch-and-swell structures are observed, creating isolated lenses of granite elongate along the foliation. These granite trails usually display mm-width biotite-rich (> 50 vol%) selvedges (Fig. 2a, c, d). Quartz-rich rafts (i.e., quartzite mylonite; Fig. 2h) embedded in glimmerite schist form bodies of more than 10 m in length and up to 50 cm in width. The study site is dominated by metre-scale layers of glimmerite schist (Fig. 2b) composed of a matrix of dominantly biotite (~50 vol%) with up to ~30 vol% of quartz, muscovite (~10 vol%) and sillimanite (~1 vol%), with isolated or clustered, coarse (up to 2–3 cm across) near-euhedral K-feldspar making up the remaining mineralogical fraction (up to 30 vol%; Fig. 2e–g). The latter form discontinuous trails along the foliation (Fig. 2a, b, e–g). The glimmerite component is observed to partially replace and disaggregate quartzite mylonite rafts along fractures (black and white arrow; Fig. 2h) (Silva *et al.,* 2022). Similar rock modification to glimmerite is observed in a range of rock types including felsic granulite and granitic gneiss (Fig. 2a–d).

3. METHOD OF ANALYSIS

3.1. Petrography and quantitative orientation analysis

Sample mineral observations were made on polished thin sections cut in the structural XZ plane using a petrographic microscope, the Virtual Petrographic Microscope (Tetley & Daczko, 2014) and ImageJ 1.47v (Rasband, 1997–2018). Mineral abbreviations follow Whitney & Evans (2010). Microstructural/crystallographic characterisation of thin sections was performed using a FEI Quanta 650 FEG-ESEM with AZtec software and an Oxford/HKL Nordlys S EBSD system at the University of Leeds, UK. EBSD mapping was performed, covering a large area of the thin section and small individual maps in specific regions of the sample, recording the mineral EDS spectra along with the EBSD data. Working conditions were: 20 kV accelerating voltage, 20–26 mm working distance, 70° specimen tilt and step size between 6 and 12 µm depending on the area covered and grain size. Automatic indexation was performed using AZtec software (Oxford Instruments). HKL Channel 5 and AZtecCrystal software (Oxford Instruments) were used to execute standard noise reduction and to extrapolate missing data using at least and in succession 8, 7, 6 and finally 5 identical neighbours with similar orientation. Grain orientation maps using Euler angles and an inverse pole figure (IPF) colour coding were generated using MTEX and HKL Channel 5 software (Bachmann *et al.,* 2010; Henry *et al.,* 2017; Henry, 2018). Presented maps include grain boundaries, defined as a boundary with a misorientation above 10°, and dauphine twin boundaries for quartz, defined as a 60° misorientation around the c-axis. The presence and character of crystallographic preferred orientation (CPO) of quartz and K-feldspar was assessed using pole figures plotted on the lower hemisphere with one point per grain. To quantify the intensity of the CPO, J-index (i.e., second-moment distribution of discrete crystal orientation data in Euler angle space (Bunge, 2013)) and M-index (i.e., distribution of uncorrelated misorientation angles (Skemer *et al.,* 2005)) are presented. Grain internal deformation is assessed by plotting the change in crystallographic orientation relative to a reference orientation.

In should be noted, that the majority of the non-indexed sectors in EBSD maps (black regions) are dominated by non-indexed biotite and lesser muscovite, as informed by petrographic microscopy.

3.2. Imaging and geochemical analysis

Micro X-ray Fluorescence (µ-XRF) analysis of the polished thin sections was used for mineral identification, spatial distribution mapping and quantification of modal proportions. µ-XRF analyses were performed using the Bruker M4 Tornado spectrometer at Macquarie University Geoanalytical (MQGA), Sydney, Australia. The µ-XRF analyses were run with a tube voltage of 50 kV, a beam current of 200 µA, a chamber pressure of 20 mbar, an acquisition time of 15 ms/pixel and using a step size of 25 µm. AMICS (Advanced Mineral Identification and Characterization System) was used to convert the X-ray fluorescence spectra to produce detailed mineral maps.

Backscatter Electron (BSE) images and *associated EDS point analyses* were used for both mineral identification and imaging of microstructures. Polished thin sections were carbon-coated and imaged in a Hitachi Desktop Scanning Electron Microscope (SEM) at the OptoFab node of the Australian National Fabrication Facility, Macquarie University, Sydney, Australia. The operating conditions of the SEM were low vacuum and 15 kV accelerating voltage. A large area BSE scan of the thin section was performed using the FEI 650 ESEM at the University of Tasmania, Australia, at low vacuum and 20 kV accelerating voltage.

Electron microprobe analyses (EMPA) acquired compositional data of silicates using a JEOL JXA 8530F Plus field emission electron microprobe at the Central Science Laboratory, University of Tasmania. The instrument is equipped with a field emission source, running an accelerating voltage of 15 kV, a beam current of 15 nA and a beam size of 10 µm. The instrument has 5 wavelength dispersive spectrometers and is operated using the Probe Software Inc. "Probe For EPMA" software package. Plagioclase Lake County, Hornblende Kakanui, Augite Kakanui, Pyrope Kakanui, Olivine Springwater, Garnet Roberts Victor Mine (all Smithsonian; Jarosewich *et al.,* 1980) and Orthoclase from P&H Developments UK were analysed as secondary standards to confirm the quality of the analysis of the unknown material. A time-dependent intensity correction was applied on Na and K if applicable. Oxygen was calculated by cation stoichiometry and included in the matrix correction. Hydrogen was calculated based on the mineral formula and included in the matrix correction as well. The matrix correction algorithm utilised was Armstrong/Love Scott (Armstrong, 1988) and the mass absorption coefficients dataset was LINEMU < 10 keV (Henke, 1985) and CITZMU > 10 keV (Heinrich, 1966). Recalculated formulae for biotite and feldspar were made based on 22 and 16 oxygens, respectively (Table 1).

Laser Ablation Inductively Coupled Plasma Mass Spectrometry (LA-ICP-MS) was used to collect data for concentration of rare earth elements in K-feldspar in thin section using a Teledyne Analyte Excite 193 nm excimer laser coupled to an 7700x ICP-MS housed at Macquarie University Geoanalytical (MQGA), Sydney, Australia. Data was collected from thin sections using 60 seconds ablation at 10 Hz, 5 J/cm^2 fluence and spot size of 150 µm. Silicon (measured by EMP) was used as an internal standard for all minerals, and NIST 610 and 612, and basalt from the Columbia River (BCR-2) were used as external standards. The raw data signal was reduced using the GLITTER software (Griffin *et al.,* 2008).

Biotite thermometry

Temperature conditions for each sample are estimated using the titanium-in-biotite thermometer of Henry *et al.* (2005). The geothermometer is based on the titanium atoms per formula unit (Ti a.p.f.u.) composition of biotite in a peraluminous metapelite with Ti-bearing minerals (ilmenite or rutile) and graphite in the mineral assemblage, equilibrated at 4–6 kbar. Temperature estimates are made by using the concentration of Ti, Fe and Mg a.p.f.u. in biotite present in a glimmerite schist sample (Table 1). Taking the experimental conditions for the geothermometer (Henry *et al.,* 2005) into account, the expected accuracy of the temperature estimates is around ± 50°C and represent minimum temperatures based on the absence of graphite and accessory Ti-bearing minerals in the studied samples (Fig. S1).

4. RESULTS

4.1. Rationale for sample selection and analyses

Since we are specifically interested in identifying cryptic signatures, we investigated samples for the chemical and microstructural evidence "left behind" during the passage of melt. We selected two representative samples exhibiting direct field evidence of melt passage through granitic gneiss (i.e., gneiss containing granitic lenses; Fig. 2a, c, d; coordinates 23.14523°S, 134.56708°E, WGS84). The samples either have mm-wide biotite selvedges (GD1617; Fig. 3a, right sample) or a lack thereof (GD1620A; Fig. 3a, left sample) at the interface of lens to granitic gneiss. For the cryptic evidence of former melt presence, we investigated a representative glimmerite schist sample (sample GD1606) with enclosed coarse K-feldspar grains (Fig. 2b, e–g; coordinates 23.14694°S, 134.56517°E, WGS84). Characterisation of the mineral chemical composition and microstructure of mainly quartz and K-feldspar was performed to resolve the geochemical and deformation processes involved in the formation of the granitic lenses and the origin of K-feldspar grains enclosed in glimmerite.

4.2. General sample description

4.2.1. Granitic lenses

Granitic lenses from samples GD1620A and GD1617 feature a high vol% of interlocked K-feldspar grains (> 75%) with apparent subhedral habit and dimensions of 3–4 mm (GD1620A) and 1–3 mm (GD1617), and interstitial quartz grains of varied dimensions (Fig. 3). Thin interstitial grain boundary films of quartz and plagioclase are observed between coarse K-feldspar grains in sample GD1620A (Fig. 3c). The minor development of sub-grains in quartz and microcline with cross-hatched crystal twinning in K-feldspar is observed in both samples (Fig. 3b, c, e). In the modified granitic gneiss, biotite grains show a gradual increase in parallel orientation towards the contact to the granitic lens (Fig. 3b). This contrasts with the cm-scale glimmerite selvedge of sample GD1617, were biotite exhibits a strong shape and crystallographic preferred orientation (Fig. 3e).

Biotite grains lack typical solid-state internal deformation microstructures (e.g., kinking or folding, recrystallisation; black and white arrows in Fig. 3e). Biotite grains protrude into relict quartz grains forming embayments (Fig. 3e). Quartz grains form low apparent dihedral angles between two biotite grains and appear as thin interstitial bands in both samples (Fig. 3d, e).

4.2.2. Glimmerite with K-feldspar grains

The glimmerite schist is characterised by three main grain sizes, with the matrix dominated by fine-grained biotite (Bt; ~50 vol% of matrix), medium-grained quartz (Qz; ~30 vol% of matrix) and muscovite (Ms; ~10vol% of matrix), and interspersed coarse-grained K-feldspar grains (Kfs; ~30 vol% of sample) (Fig. 4a, d). The remaining glimmerite schist matrix is constituted by sillimanite (Sil; ~1 vol%) and ~9 vol% of a very fine-grained Al-Si-rich alteration product after aluminosilicates, mainly sillimanite and feldspars, and inferred to be kaolinite or pyrophyllite associated with late-stage local retrogression (labelled on as Alt. on figures), that fills grain micro-fractures (Fig. 4a, d, e). Small and minor plagioclase grains show preferential spatial arrangement near to and/or in contact with K-feldspar grains as small rims and occasionally in thin embayments (Fig. 5a, b). Due to the presence of the latter alteration product, we note that in the pre-alteration rock, the mode of sillimanite may have been higher, and plagioclase may have comprised a significant proportion of the assemblage. Minor proportions (< 1 vol%) of magnetite (~0.04 vol%), apatite (~0.017 vol%), monazite (~0.015 vol%) and zircon (~0.014 vol%) are observed in the matrix which is otherwise dominated by biotite and quartz.

The minerals in the rocks exhibit a strong shape preferred orientation, where coarse K-feldspar grains, biotite grains and bands of quartz grains are aligned parallel to the main lineation and lie in the foliation (S-plane; Berthé *et al.,* 1979) of the rock (Fig. 4a, b). Bands of quartz grains and biotite are not only seen parallel to the glimmerite schist foliation but may also form bands oriented at 45° relative to the foliation (C'-type shear bands; Berthé *et al.,* 1979) (Fig. 4a, b). Similar to the biotite grains in the selvedges from sample GD1617, biotite grains lack kinking, folding or recrystallisation microstructures (Figs. 4b, c, and 5e, f). The coarse K-feldspar grains show (i) little evidence of crystal-plastic deformation (i.e., lack undulose extinction; Fig. 4a–c), (ii) apparent subhedral shape (i.e., semi-straight crystal faces; Fig. 4a–e), (iii) lack recrystallisation around the grain edges (i.e., lack core-mantle microstructure common in high-strain mylonite; Fig. 4e), and (iv) display fractures filled by fine-grained Al-Si-rich alteration product (Fig. 4e). Most coarse K-feldspar grains exhibit quartz inclusions (Fig. 4d, e), with plagioclase being less common (Fig. 5a) and one coarse K-feldspar grain shows a monazite inclusion (Fig. 4e). Biotite, sillimanite, and small quartz grains are observed to wrap around and form tails of matrix minerals at the extremities of the coarse K-feldspar and muscovite grains (Figs. 4e and 5c–e). Agglomerates of smaller quartz and feldspar grains, together with minor biotite, are visible in areas between the aligned coarse K-feldspar grains (i.e., in the strain shadows; Figs. 4d, e and 5b). The agglomerates of quartz and K-feldspar are irregularly-shaped and interstitial to the coarse K-feldspar (Figs. 4e and 5b). These small K-feldspar and quartz grains lack evidence for significant crystal-plastic deformation, i.e., they lack undulose extinction, subgrains and recrystallised grains (Figs. 4e and 5b).

4.3. Mineral chemistry

In the feldspar solid solution ternary plot (Fig. 6), the coarse K-feldspar grains present within glimmerite schist show a slightly variable composition within the 80–90 mol% orthoclase range. Analyses performed at the rim of the K-feldspar grains show an increase in orthoclase component (Figs. 4e and 6). In the same glimmerite sample, relict plagioclase (partially altered to Si-Al alteration product in fractures) have almost pure albite composition (Figs. 4e, 5a, b and 6).

To investigate the temperature of growth, titanium-in-biotite thermometry (Henry *et al.,* 2005) was performed on biotite in the main glimmerite schist (sample GD1606; Fig. 2e, f). Ti a.p.f.u. values are recorded in the range of 0.11–0.15 a.p.f.u with most of the values concentrated above 0.13 a.p.f.u (TiO_2 values of 2.03–2.63 wt%; Table S1). Biotite X_{Mg} values are recorded in the range of 0.53–0.58 a.p.f.u and mostly concentred up to 0.56 a.p.f.u (Fe: 16.25–17.82 wt%; Mg: 11.32–

12.55 wt%; Table S1) (Fig. S1). The calculated Ti concentration in biotite from glimmerite schist reflects an apparent temperature of growth of ~660 ± 50°C.

Coarse and interstitial K-feldspar grains from the glimmerite schist (sample GD1606; Fig. 4e and 5b; see also Fig. 10) have an overall enriched REE pattern compared to chondrite REE values (McDonough & Sun, 1995), with La > Lu and a progressive depletion pattern from La to Sm (Fig. 7a). From Gd to Lu, a faint concave-up shaped REE pattern is observed. Coarse K-feldspar grains have a slight increase in Eu in spot analyses located close to the rim of the grains (Fig. 7c). K-feldspar grains in the granitic lens (sample GD1620A) present a much higher variability in REE concentration between grains compared to those in the glimmerite schist (Fig. 7a). K-feldspar grains from both rock types display positive Eu anomalies except for one enriched grain within the granitic lens that shows a modest negative Eu pattern slope. Compiled data of K-feldspar REE values from rock types analogous to the samples analysed in this study show similarities to our analysed K-feldspars in granitic lens and glimmerite schist (Fig. 7a, b). The variability in REE patterns is most intense in the K-feldspar in granodiorite gneiss (Bingen *et al.,* 1990), followed by the K-feldspar-rich leucosome (Carvalho *et al.,* 2016) and lastly K-feldspar in pegmatite (Larsen, 2002).

4.4. Detailed microstructures and crystallographic orientation relationships

There are several mineralogically distinct bands at ~45° to the stretching lineation (Fig. 4a, 8). These are composed mainly of K-feldspar or quartz grains within an aggregate of K-feldspar, quartz and biotite of sigmoidal shape, specifically in between two C'-type planes forming a biotite shear band in thin section (Fig. 4a). The elongation of quartz grains is observed to follow the sigmoidal shapes of the mica fabric (in Fig. 8a black areas) and individual quartz grains apparently bend around K-feldspar grains, yet show little internal deformation (Fig. 8b). The quartz [c]-axis maximum presents a relatively weak and broad cluster (max. 2.6 mean angular deviation) parallel to the Z-axis and <a> axes are scattered along a pole figure primitive circle (Fig. 8c). Both J- and M-indices are low with 1.27 and 0.02, respectively. Pole figures for K-feldspar are presented in two groups divided by grain size. The threshold for the division in coarse K-feldspar and interpreted interstitial grains was set at 0.5% of the map area. The group of identified coarse K-feldspar grains moderately clustered a-axes around the Z-axis and c-axes are clustered in the SW sector close to the primitive circle, similar in orientation to the C'-type shear bands displayed in Fig. 8a. Interstitial K-feldspar grains show some alignment with a J- and M-index of 2.44 and 0.03, respectively (Fig. 8c). K-feldspar shows [c]-axis orientations dispersed 45° at the top and bottom on the X-axis pole figure. The distribution of misorientation between pairs of quartz and K-feldspar shows nearly perfect random distribution for quartz grains and weak correlation of misorientation distribution for K-feldspar grains below 60° (Fig. 8c).

There are no internal changes to crystal orientation within the coarse K-feldspar grains, nor are there any sub-grains present within the rims of the grains (Fig. 9). K-feldspar grains still preserve relatively straight grains boundaries (crystal facets) when comparing the inferred boundaries to a 3-dimensional representation of the grain orientation and crystallographic system (coloured dashed lines; Fig. 9). Biotite and muscovite commonly protrude into the K-feldspar in the glimmerite schist (Fig. 5a, c, e). These mica embayments are observed to preferentially follow the direction of the crystal axes i.e., perpendicular to the crystal planes, of the K-feldspar grains (coloured arrows; Fig. 9).

In the low-strain areas between the aligned K-feldspar grains, quartz grains exhibit extensive formation of Dauphine twin boundaries (Fig. 10a), while the K-feldspar grains of all grain sizes do not present any significant misorientation within individual grains (Fig. 10b). Similar to the K-feldspar in Fig. 9, no sub-grain boundaries are observed. Two coarse interstitial quartz grains, separated in 2-dimensions by the clustered small K-feldspar grains, present a misorientation between them of less than 15° (Fig. 10a). Most of the clustered small K-feldspar grains exhibit similar characteristics to the coarse K-feldspar grains (see Fig. 9) with limited crystal lattice bending, relatively straight grain boundaries and biotite protrusions along the K-feldspar a, b and c axes (Fig. 10b). Two small K-feldspar grains that exhibit similar orientation are shown in Fig. 10b (pink grains).

Both these grains share grain boundaries with other small K-feldspar grains. The array of small K-feldspar grains in the strain shadow of the coarse K-feldspar grains share similar orientations (green colours on Fig. 10a inset), while the surrounding coarse K-feldspar grains also share a similar orientation to each other (pink colours on Fig. 10a inset), but different to the small interstitial grains.

5. DISCUSSION

Recent studies of the Alice Springs Orogeny and the Gough Dam shear zone show that high-strain zones are characterised by (1) prevalent microstructures indicative of the former presence of melt; (2) lack of plastic deformation and CPO in quartz; (3) an inferred correlation between increased time-integrated melt flux and increased temperature of biotite formation, along with increased REE and trace elements concentration, and (4) a complex monazite age pattern due to coupled dissolution-precipitation reactions mediated by interaction with melt (Piazolo *et al*., 2020; Silva *et al*., 2022). These studies further propose that the abundant glimmerite bands formed by hydration and addition of various elements, mostly K and Al, and in a lesser amount Na, Mg and Fe, during melt-rock interaction and the passage of melt through the GDSZ. The extent of melt-rock interaction forming glimmerite is controlled by the variability of (i) the composition of the melt source, (ii) extent of geochemical modification of the melt during reactive flow due to channel armouring, (iii) variation in rock types interacted along melt migration pathways, and (iv) possible trapping of early crystallised minerals (i.e., phenocrysts in the migrating melts) during the collapse of pathways as melt supply is reduced. Silva *et al*. (2022) calculated minimum time-integrated melt flux volumes of 0.03–0.23m^3 of melt per m^3 of rock, indicating large volumes of melt migrated through high-strain zones during the Alice Springs Orogeny. Recent work investigating the enrichment of oxide minerals in a high-strain zone immediately south of the GDSZ also inferred large volumes of melt are required to migrate through the high-strain zones in order to explain the observed enrichment (Ghatak, *et al*., 2022). Furthermore, the presence of melt during deformation in the GDSZ weakened the high-strain zone rheologically enhancing exhumation throughout the Alice Springs

Orogeny. While this study complements the previous research by examination and characterisation of granitic lenses and other felsic components associated with hydration reactions forming glimmerite, our focus here is to establish if the presence of coarse, faceted K-feldspar grains within the glimmerite is a direct consequence of melt flux during deformation. If true, then such K-feldspar grains represent a new indicator of the former presence of syntectonic and migrating melts.

5.1 Syntectonic melt migration: From field to petrographic and microstructural evidence

At the macro-scale, field relationships show both the biotite-rich and the biotite-poor rocks have features typical of melt-present high-strain zones: (i) preferential mineral alignment forming a distinct and well-developed foliation and lineation defined mainly by biotite and facetted K-feldspar grains; (ii) lenses with granitic composition and coarse grains aligned along the foliation resemble pinch and swell patterns; and (iii) elongated grains of quartz and feldspar in granitic gneisses, with some K-feldspar grains exhibiting sigmoidal shapes (Fig. 2; Vernon, 1987; Lister & Snoke, 1984; Passchier & Trouw, 2005). Although commonly formed during solid-state deformation, the alignment of biotite or K-feldspar grains can also be produced by magmatic flow (Collins & Sawyer, 1996; Paterson *et al.,* 1998; Vernon, 2000; Žák *et al.,* 2008; Zibra *et al.,* 2014). Close examination of the granitic lenses shows that these present igneous characteristics including interlocking, faceted feldspar grains of unimodal grain size, and interstitial quartz and plagioclase (Figs. 2c, d and 3). Even though the trails of granitic lenses resemble pinch and swell structures, the minerals constituting the lenses show little evidence for solid-state deformation (e.g., bimodal grains size or mantled porphyroclast observed by, for example, Vernon *et al.* (1983) and Tullis & Yund (1991)). There is a lack of evidence for solid-state deformation in the granitic lenses, such as dynamic recrystallisation, (e.g., Kruse & Stünitz, 1999; Svahnberg & Piazolo, 2010) (Fig. 3b–e) which points toward a differential stress regime synchronous with melt injection. The geometric shape and arrangement of granitic lenses closely resemble the pseudo-boudinage of Bons *et al.* (2004) and Druguet & Carreras (2006), in which they describe similar patterns resembling pinch and swell structures in partially crystallised pegmatites. Importantly, the facetted nature of K-feldspar grains within granitic lenses (Fig. 3) is consistent with an igneous origin without significant post-crystallisation internal deformation or modification. This is a feature common to many high melt volume migmatites (Sawyer, 2008).

In the field, the schistose nature of the glimmerite (Fig. 2e–h) suggests grain alignment of all key minerals in the assemblage. This is supported by petrographic evidence for preferential grain alignment of biotite, K-feldspar, quartz, muscovite and sillimanite (Figs. 4 and 5). Differential stress is interpreted to cause preferential mineral alignment and polymineralic sigmoidal shaped structures comprising a combination of muscovite, K-feldspar and quartz (Fig. 4d; Passchier & Trouw, 2005), and biotite shear bands (C'-type; Berthé *et al.,* 1979) at ~45° to the foliation (Figs. 4a and 8a). However, close analysis of the minerals highlights very limited internal grain deformation and a distinct lack of features commonly observed in high-strain zones that deform in the solid-state (e.g., kinking and folding of biotite and/or undulose extinction in K-feldspar and quartz grains (Figs. 4a and 5e, f) (e.g., Wilson, 1980; Lister & Snoke, 1984). Development of mica fish, grain size reduction producing core-mantle structures and internal deformation structures such as subgrain boundaries and continuous crystal lattice bending, commonly attributed to solid-state crystal-plastic deformation (e.g., Ten Grotenhuis *et al.,* 2003; Passchier & Trouw, 2005; Mancktelow & Pennacchioni, 2005), are completely missing from the glimmerite schist (Figs. 4 and 5).

We suggest that the absence of a strain record in the individual grains comprising the glimmerite schist and granitic lenses is consistent with the presence of a weak intergranular medium, in this case, interstitial melt that accommodated a large part of the applied stresses via grain boundary sliding. This is similar to the experimental aggregate strength reduction with the increase of melt fraction in mylonites from Rosenberg & Handy (2005). Our model of melt-present deformation is supported by the following microstructures in the different samples described. At the edge of the granitic lenses, the described highly elongate grains of plagioclase and quartz (Fig. 3b, c) are interpreted as minerals that pseudomorphed grain boundary melt films (Holness & Sawyer, 2008). In the glimmerite schist, melt–K-feldspar reaction can account for the presence of embayments containing plagioclase, biotite and muscovite at the edge of coarse K-feldspar grains (Figs. 4e, 5a, c, 9 and 10b). These embayment reactions resemble a “back reaction” of the vapour absent melting reaction: Ms + Qz + Pl = Kfs + Sil (or Ky) + Melt (Patiño Douce & Johnston, 1991). The quartz and K-feldspar aggregates in the low-strain shadows between the coarse K-feldspar grains closely resemble interstitial textures, consistent with melt-present deformation (Figs. 4a, d, e, 5b, c and 10). The observation of weak CPO of quartz and K-feldspar, even though there is a strong foliation and lineation, contradicts the common observation of high CPO intensity in solid-state crystal plastic deformation at high strain (e.g., Lister & Hobbs, 1980; Law, 1990; Menegon *et al.,* 2008; Law *et al*., 2010). However, this conundrum can be explained by the presence of melt during deformation which accommodated most of the strain. In the low-pressure or strain shadow regions between coarse K-feldspar grains, a trail of smaller K-feldspar grains resembling a deformation tail is observed (Figs. 4e, 5b and 10). This type of microstructure is commonly observed in deformed porphyroclasts present in mylonite. However, in the latter scenario, the tails comprise recrystallised material from the porphyroclast or the strain shadows comprise minerals formed by solid state crystal plasticity (i.e., dynamic recrystallisation) or dissolution-precipitation mechanisms, respectively (Yardley, 1977; Vernon, 1987; Passchier & Trouw, 2005). Although resembling a deformation trail by dynamic recrystallisation, the smaller K-feldspar trail does not present microstructures indicative of such a process. This interpretation is informed by the lack of internal deformation and sub-grain formation close to the coarse K-feldspar grain boundaries (Fig. 10) (Tullis & Yund, 1985; Ree *et al.,* 2005; Menegon *et al.,* 2008, 2013). By contrast, some of the smaller isolated K-feldspar grains in the low-pressure regions are connected in three dimensions, as they share the same crystallographic orientation, indicating crystallisation from grain-boundary melt connected in 3D (Fig. 10b).

In addition, the microstructure of the embayments into the coarse K-feldspar grains is unusual for a high-strain rock deformed by solid-state deformation (Passchier & Trouw, 2005; Figs. 9 and 10b). In the latter case, one would expect interlocking microstructure between these minerals.

Instead, a reactive nature of that contact, where K-feldspar is dissolved, and plagioclase-biotite-muscovite grow is more likely. The fact that this texture is undeformed but still aligned with the general foliation of the sample suggests formation at a time the rock was under differential stress. We suggest that this microstructure formed when melt-K-feldspar interaction triggered the dissolution of K-feldspar and precipitation of plagioclase-biotite-muscovite. This indicates that the melt involved in the reaction was different to that from which the K-feldspar grew, consistent with open system melt flux through the high-strain zone.

The low mode of quartz in the granitic lenses and in the glimmerite schist suggests that the silica-rich interstitial melt was physically removed from the system. Melt expulsion is caused by waning melt pressure relative to confining pressure and/or differential tectonic stress (Davidson *et al*., 1992, 1994; D'lemos *et al.*, 1992; Brown, 1994). In summary, the microstructures observed in the rocks of the GDSZ are consistent with high-strain melt-present deformation.

5.2. Origin of the coarse K-feldspar grains within glimmerite

The coarse K-feldspar grains observed as dominantly individual grains in the glimmerite schist are interpreted to have formed by early, ex-situ crystallisation of the interpreted migrating granite melt (Figs. 2e–g and 4). Other examples of concentration of K-feldspar are described in the literature (e.g., in granitoids [e.g., Vernon, 1986; Vernon & Paterson, 2008], in schlieren suggesting phenocryst flow-sorting [e.g., Bateman & Chappell, 1979; Vernon, 1986], and in enclaves in megacrystic granitoids [e.g., Didier, 1973]). The igneous origin of K-feldspar grains is further supported by the similarities between the K-feldspar grains of the granitic lenses which are of igneous origin, and the K-feldspar within the glimmerite. Similarities between K-feldspar grains in these two rocks include coarse grain size, conservation of faceted grains, low internal deformation and rare presence of small inclusions (Figs. 3–5).

The observed matrix foliation wrapping around the K-feldspar grains indicates pre- to syntectonic mineral growth, in our case in migrating granitic melt similar in composition to the previously described granitic lenses (Figs. 4e and 5). Porphyroblasts in high-strain zones share this characteristic and may also exhibit inclusion trails or sigmoidal shape commonly showing grain rotation relative to the matrix foliation (Passchier *et al.,* 1992; Johnson, 1999). We use (1) the foliation warping around the K-feldspar grains in addition to (2) preservation of crystal faces, (3) lack of internal deformation and (4) lack of core-mantle microstructure, features indicating recrystallisation by grain area reduction (Figs. 4e, 5, 9 and 10; see review of these microstructures in Passchier & Trouw (2005) and Blenkinsop (2007)) to interpret the K-feldspar grains as early crystallising minerals from the migrating melt. Following the described physical characteristics of the K-feldspar grains, an alternative peritectic origin could be suggested for the formation of the K-feldspar phenocrysts (e.g., Sawyer, 2008; Cruciani *et al.*, 2008; Vernon, 2011; Dyck *et al.*, 2020). However, the peritectic hypothesis is problematic when related to the following description of the K-feldspar microstructures and reaction with entrapped melt. The shape of the K-feldspar has been weakly modified to form the embayments by reaction replacement producing plagioclase, biotite and muscovite that we interpret as due to grain–melt reaction subsequent to the K-feldspar grains being entrapped (Figs. 5a, 9 and 10b). The presence of entrapped melt is also observed in the granitic lenses in the form of elongated interstitial plagioclase (Fig. 3c). It is apparent that reaction dissolution was enhanced along the crystallographic b and c axes of the K-feldspar phenocrysts, similar in concept to the observed forsterite anisotropic dissolution favouring crystallographic axes (Grandstaff, 1978; Awad *et al.,* 2000; Godinho *et al.,* 2013, 2014) or the preferential partial melting along subgrain boundaries in quartz and plagioclase of Levine *et al.* (2016).

The K-feldspar grains exhibit no evident chemical zonation, except for some rim domains showing a localised stronger positive Eu anomaly and a slight increase in orthoclase component (Figs. 6 and 7c). This limited chemical zonation suggests that the crystallisation of the K-feldspar grain in the migrating melt was fast, and that the crystallisation of melt was of short duration. This model of K-feldspar crystallisation is informed by the tendency of feldspar grains to form chemical zonation due to the strength of the Si-O and Al-O bonds (Winter, 2013) and/or by an open system allowing the chemical or physical disruption of the boundary layer around the K-feldspar grain which is usually depleted in elements with mineral/melt partition coefficient > 1, allowing maximum crystal growth (Green & Watson, 1982; Bacon, 1989). The fast growth of the K-feldspar phenocrysts can be explained by reduced nucleation in highly hydrous silicate melts, as per the crystallisation mechanism of the igneous K-feldspar grains in the surrounding granitic lenses (Figs. 2a, c and 3). Once the mineral nucleates, fast mineral growth occurs at undercooled conditions (Nabelek *et al.,* 2010). The fast growth surrounded by melt allied to delayed nucleation possibly explains the rarity of small inclusions in K-feldspar grains and phenocrysts in both the glimmerite and granitic lenses (Figs. 3b–e, 5, 9 and 10). In experimental conditions, K-feldspar crystallisation begins with at least 60–70% of liquid in the crystal mush which may suggest that the phenocrysts grew in pockets of the fluxing melt with a high fraction of liquid (Clemens & Wall, 1981; Winkler & Schultes, 1982). The crystallisation of K-feldspar first is per the observed sequence of mineral crystallisation in granite, as extensively discussed by Vernon & Paterson (2008) for K-feldspar megacrysts in granite and zoned pegmatites that tend to form monomineralic segregations of K-feldspar or quartz, starting far from the liquidus with an initial assemblage of K-feldspar + quartz ± biotite (Cameron *et al.,* 1949; London, 2005). This may suggest that the melt migrating through the GDSZ may have had a chemical composition close to the aforementioned zoned pegmatites and the observed GDSZ granitic lenses due to the similarities in the observed sequence of mineral crystallisation (Fig. 3).

Some K-feldspar grains exhibit an increase in Eu and modal component of orthoclase at the rim of the grain (Figs. 6 and 7a, c). This increase in Eu concentration and orthoclase component occurs close to the embayments into the K-feldspar grains, suggesting that the contact with a subsequent melt triggers localised "back reaction", discussed previously. This may locally modify the Eu concentration in the K-feldspar due to the high Kfs/melt Eu partition coefficient; the higher orthoclase component may be due to coupled exchange of Na and K at the reaction interface during formation of albite (Labotka *et al.,* 2004; Hövelmann *et al.,* 2010). The REE concentrations of the K-feldspar in the granitic lenses show highly variable values between grains (Table 2 and Fig. 7a). This variability contrasts with the mainly homogeneous REE pattern and enriched REE concentration of K-feldspar in glimmerite schist (this study), magmatic K-feldspar in pegmatite and porphyroblastic K-feldspar in granodiorite gneiss (Fig. 7b) (Larsen, 2002; Bingen *et al.,* 1990). However, the variability in REE concentration values and overall patterns in the granitic lenses resembles the REE patterns observed for migmatites in leucosome from Carvalho *et al.* (2016). This variability in REE concentration values between grains can be explained by higher fractional crystallisation of K-feldspar grains due to lower melt flow while mineral crystallisation occurred. The progressively decreasing REE pattern of the K-feldspar from La to Lu in the glimmerite schist resembles the patterns observed for some of the pegmatite K-feldspar and migmatite leucosome data (Fig. 7b). K-feldspar grains in leucosome (Carvalho *et al.,* 2016) show depleted HREE compared to our K-feldspar phenocrysts. This is explained by melt flow entrainment of accessory minerals with high HREE affinity from the adjacent rock. The contrast in REE patterns suggests that this physical process is unlikely to have taken place in the channelised melt flow forming the K-feldspar phenocrysts here. The similarity in REE concentration pattern with pegmatites and migmatite leucosome is consistent with a magmatic origin for the K-feldspar present in the glimmerite schist and our preserved phenocryst interpretation.

5.3. Trapped K-feldspar: A signature for melt fluxing and subsequent melt extraction and associated physical collapse

Following our interpretation of melt-present deformation in the GDSZ and supported by similar conclusions by Piazolo *et al.* (2020) and Silva *et al.* (2022), and that the K-feldspar has an igneous origin, one question remains: how did relatively undeformed K-feldspar grains end up in a high-strain zone? We interpret a prolonged one-step process where the K-feldspar phenocrysts crystallised in the channelised migrating melt and were trapped in the glimmerite schist during the collapse of the melt pathways. We infer that a decrease in the melt supply (i.e., draining of the source), implying a waning of the melt pressure, meant that the melt pressure could no longer maintain an open channel while confining pressure and tectonic stress were still significant, leading to the structural collapse of the system (e.g., Kisters *et al.*, 2009; Fig. 11).

In our model, we interpret the melt filling of tensional fractures along strike, possibly formed due to an anisotropic tensile strength of the protolith (Wickham, 1987), as the most probable mechanism for the initiation of the melt pathways observed in the study area. Additionally, the physical size of the K-feldspar grains also argues against a more pervasive grain boundary melt flow process that would have formed interconnected melt flow bands (Fig. 2a, c, d) (Brown, 1994; Weinberg, 1999; Bons *et al.,* 2004). Other indications of fracture propagation are observed in the orthogonal mode 1 extensional fractures in the quartzite mylonite layers surrounded by the glimmerite schist (Fig. 2h). The same development of pathways is believed to have happened early in the formation of the glimmerite schist. These pathways are not as visible in the glimmerite rock type due to the higher amount of melt-rock interaction producing glimmerite at the expense of adjacent rocks by dissolution-precipitation (Fig. 2b, h; Silva *et al.*, 2022). Furthermore, the grain shape and preferred orientation of the micas possibly facilitated the extraction of melt during the collapse of the high-strain zone (Figs. 4 and 5) (Weinberg *et al.,* 2001; Žák *et al.,* 2008). The presence of a melt fraction in the glimmerite schist during the period of deformation would have decreased the strength of the rock by several orders of magnitude and increased the temperature of biotite formation compared to the glimmerite bands adjacent to the modified granulite rocks (Fig. S1) (Rosenberg & Handy, 2005; Silva *et al.*, 2022). Extreme weakening increases non-linearly up to 10 vol% of melt fraction (melt connectivity transition of Rosenberg & Handy (2005)), with the melt lubricating 90% of crystal boundaries at the 10 vol% melt fraction threshold described by Van der Molen & Paterson (1979).

The final melt extraction and crystal entrapment occurred during the collapse of the high-strain zone when the combined confining pressure and tectonic stress finally overcame the melt pressure. The proposed formation of the trails of granitic lenses observed in the felsic bands (Fig. 2a, c, d) follow closely the model of Bons *et al*. (2004) and Druguet & Carreras (2006) for their syntectonic melt deformation, inflation and collapse of pegmatite dykes in Cap de Creus, Spain. In Bons *et al.* (2004), one of the main features used to recognise collapse structures is the formation of thinning beads (Fig. 9a in Bons *et al.,* 2004) in partially crystallised pegmatite dykes. These can easily be interpreted as boudinage, in lieu of formation of collapse beads, due to the morphological similarities at outcrop scale (Bons *et al.,* 2004, 2008; Druguet & Carreras, 2006). During the process of collapse, most of the strain and foliation deflection is localised at the corner of the beads, decreasing away from these structures. These observations are at odds with the observed strain spanning the entire area in between boudins. Furthermore, no evidence of dyke-parallel stretching within the beads or in the thin seams connecting the beads are observed when pegmatite beads form by local inflation and collapse, usually observed in boudin formation (Bons *et al.,* 2004).

The overall main characteristics of the beads formation model of Bons *et al.* (2004, 2008) fit the observed lack of extensional deformation of the granitic lenses in our study area and the small amount of strain observed in between them (Figs. 2c, d and 3). Altogether, these structural characteristics of the granitic lenses fits the concept of pseudo-boudinage. The presence of a high vol% of melt during the period of deformation of the granitic lenses most probably allowed the strain to concentrate into the melt instead of the solid mineral grains (Vigneresse & Tikoff, 1999), resulting in little internal evidence of the synchronous high strain in the remaining beads. A similar process of melt filled fractures followed by collapse is proposed for the formation of the glimmerite schist. The sequence of melt inflation and later collapse would explain the presence and entrapment of K-feldspar phenocrysts in the glimmerite matrix and the entrapment and crystallisation of melt in low-strain regions of the glimmerite schist (Figs. 2e, f, 4e and 10). This collapse process would also explain the inferred melt extraction that mitigated the formation of granitic bodies within the glimmerite schist. This is also consistent with the small number of igneous microstructures observed in the glimmerite matrix and the lack of deformation of solid grains. Following the Bons *et al.* (2004) collapse model, we suggest that the contrast between the granitic lenses and the isolated K-feldspar crystals was due to differential concentration of crystals locally present during the collapse, leading to a decrease of crystal entrapment with an increase of melt fraction.

6. CONCLUSIONS

The presence of undeformed and faceted K-feldspar phenocrysts as individual grains or clusters of grains in a high-strain zone of the Gough Dam shear zone, central Australia, occurred via the entrapment of entrained early crystallised minerals in channelised migrating melt due to the collapse of wall rocks constituting the melt pathway. The opening of melt pathways probably occurred by tensional fractures along rock anisotropies. This syndeformational creation of melt migration pathways in a high-strain zone allowed channelised melt flux, as observed by the presence of granitic lenses, and extensive melt-rock interaction. The melt-mediated reaction produced glimmerite schist and glimmerite, and involved dissolution of the adjacent felsic wall rocks. Early, fast-growing K-feldspar grains crystallised from the fluxing melt due to the delayed mineral nucleation in an undercooled and hydrous melt. The posterior collapse of the melt pathway, comprising glimmerite enriched walls, occurred following decreased melt supply. This ultimately led to the entrapment of the crystallised minerals (phenocrysts) in the melt and synchronous extraction of the remaining liquid fraction from the high-strain zone. This physical entrapment process allowed the formation of granitic lenses in less reacted melt pathways (granitic gneiss) and an increase in the efficiency of entrapment of phenocrysts in the more reacted glimmerite schist bands. We suggest the presence of undeformed K-feldspar in high-strain zones is a new indicator of the former passage of migrating melt through rock types with otherwise limited field evidence indicative of the former presence of melt during deformation.

ACKNOWLEDGMENTS

We thank the landowners for permission to access sample localities in the Gough Dam shear zone, central Australia. M. Bebbington, T. Murphy, Y-J. Lai and H. Ghatak (Macquarie University) assisted with making thin sections and geochemical analysis. Sandrin Feig (University of

Tasmania) assisted with electron microprobe analysis. Duncan Hedges and Richard Walshaw (University of Leeds) assisted with EBSD data collection. This work was carried out as part of a PhD study at Macquarie University and was supported by ARC Discovery grant DP160103449 to A. Putnis, T. Raimondo and N. Daczko. We thank R. White (University of St. Andrews) and an anonymous reviewer for constructive comments and editorial handling. We thank S. Cruden (Monash University) and A. Tommasi (University of Montpellier) for feedback on an earlier version of this manuscript. This study used instrumentation funded by ARC LIEF, DEST Systemic Infrastructure Grants, NCRIS/AuScope, industry partners and Macquarie University. This is contribution 1745 from the ARC Centre of Excellence for Core to Crust Fluid Systems (http://www.CCFS.mq.edu.au).

SUPPLEMENTARY DATA

Supplementary data are available at Journal of Metamorphic Geology online.

REFERENCES

Armstrong, J. T. (1988). Quantitative analysis of silicate and oxide materials: Comparison of Monte Carlo, ZAF, and ψ (ρz) procedures. *Microbeam Analysis*, 239–246.

Awad A., van Groos A. F. K., & Guggenheim, S. (2000). Forsteritic olivine: effect of crystallographic direction on dissolution kinetics. *Geochimica et Cosmochimica Acta, 64*(10), 1765–1772.

Bachmann, F., Hielscher, R., & Schaeben, H. (2010). Texture analysis with MTEX–free and open source software toolbox. *Solid State Phenomena*, *160*, 63–68.

Bacon, C. R. (1989). Crystallization of accessory phases in magmas by local saturation adjacent to phenocrysts. *Geochimica et Cosmochimica Acta*, *53*(5), 1055–1066.

Ballèvre, M., Hensen, B. J., & Reynard, B. (1997). Orthopyroxene-andalusite symplectites replacing cordierite in granulites from the Strangways Range (Arunta block, central Australia): a new twist to the pressure-temperature history. *Geology, 25*(3), 215–218.

Ballèvre, M., Möller, A., & Hensen, B. J. (2000). Exhumation of the lower crust during crustal shortening: an Alice Springs (380 Ma) age for a prograde amphibolite facies shear zone in the Strangways Metamorphic Complex (central Australia). *Journal of Metamorphic Geology, 18*(6), 737–747.

Bateman, P. C. & Chappell, B, W. (1979). Crystallization, fractionation, and solidification of the Tuolumne Intrusive Series, Yosemite National Park, California. *Bulletin of the Geological Society of America, 90*(5), 465–482.

Bea, F., Pereira, M. D., & Stroh, A. (1994). Mineral/leucosome trace-element partitioning in a peraluminous migmatite (a laser ablation-ICP-MS study). *Chemical Geology*, *117*(1–4), 291–312.

Beere, W. (1975). A unifying theory of the stability of penetrating liquid phases and sintering pores. *Acta Metallurgica*, *23*(1), 131–138.

Bendall, B. (2000). Mid-Palaeozoic shear zones in the Strangways Range: a record of intracratonic tectonism in the Arunta Inlier, Central Australia (Doctoral dissertation). University of Adelaide, Adelaide, Australia.

Berthé, D., Choukroune, P., & Jégouzo, P. (1979). Orthogneiss, mylonite and non coaxial deformation of granites: the example of the South Armorican Shear Zone. *Journal of Structural Geology*, *1*(1), 31–42.

Bingen, B., Demaiffe, D., & Hertogen, J. (1990). Evolution of feldspars at the amphibolite-granulite-facies transition in augen gneisses (SW Norway): geochemistry and Sr isotopes. *Contributions to Mineralogy and Petrology*, *105*(3), 275–288.

Blenkinsop, T. G. (2007). *Deformation Microstructures and Mechanisms in Minerals and Rocks*. Springer Science & Business Media.

Bons, P. D. (1999). Apparent extensional structures due to volume loss. *Proceedings Estonian Academy of Sciences, 48*, 3–14.

Bons, P. D., Becker, J. K., Elburg, M. A., & Urtson, K. (2009). Granite formation: stepwise accumulation of melt or connected networks? *Earth and Environmental Science Transactions of the Royal Society of Edinburgh*, *100*(1–2), 105–115.

Bons, P. D., Druguet, E., Castaño, L. M., & Elburg, M. A. (2008). Finding what is now not there anymore: Recognizing missing fluid and magma volumes. *Geology*, *36*(11), 851–854.

Bons, P. D., Druguet, E., Hamann, I., Carreras, J., & Passchier, C. W. (2004). Apparent boudinage in dykes. *Journal of Structural Geology*, *26*(4), 625–636.

Brown, M. (1994). The generation, segregation, ascent and emplacement of granite magma: the migmatite-to-crustally-derived granite connection in thickened orogens. *Earth-Science Reviews*, *36*(1–2), 83–130.

Brown, M. (2005). Synergistic effects of melting and deformation: an example from the Variscan belt, western France. *Geological Society, London, Special Publications*, *243*(1), 205–226.

Brown, M. & Rushmer, T. (2006). *Evolution and Differentiation of the Continental Crust*. Cambridge University Press.

Brown, M. & Solar, G. S. (1998). Shear-zone systems and melts: feedback relations and self-organization in orogenic belts. *Journal of Structural Geology, 20*(2–3), 211–227.

Buick, I. S., Storkey, A., & Williams, I. S. (2008). Timing relationships between pegmatite emplacement, metamorphism and deformation during the intra-plate Alice Springs Orogeny, central Australia. *Journal of Metamorphic Geology*, *26*(9), 915–936.

Bunge, H. J. (2013). *Texture Analysis in Materials Science: Mathematical Methods*. Elsevier.

Cameron, E. N., Jahns, R. H., McNair, A. H., & Page, L. R. (1949). Internal structure of granitic pegmatites. *Economic Geology Monograph*, *2*, 115 p.

Cartwright, I., Buick, I. S., Foster, D. A., & Lambert, D. D. (1999). Alice Springs age shear zones from the southeastern Reynolds Range, central Australia. *Australian Journal of Earth Sciences*, *46*(3), 355–363.

Carvalho, B. B., Sawyer, E. W., & Janasi, V. A. (2016). Crustal reworking in a shear zone: transformation of metagranite to migmatite. *Journal of Metamorphic Geology*, *34*(3), 237–264.

Clemens, J. D., & Wall, V. J. (1981). Origin and crystallization of some peraluminous (S-type) granitic magmas. *The Canadian Mineralogist*, *19*(1), 111–131.

Collins, W. J., & Sawyer, E. W. (1996). Pervasive granitoid magma transfer through the lower–middle crust during non-coaxial compressional deformation. *Journal of Metamorphic Geology*, *14*(5), 565–579.

Collins, W., & Shaw, R. (1995). Geochronological constraints on orogenic events in the Arunta inlier: a review. *Precambrian Research, 71*(1), 315–346.

Collins, W., & Teyssier, C. (1989). Crustal scale ductile fault systems in the Arunta inlier, central Australia. *Tectonophysics, 158*(1), 49–66.

Cruciani, G., Franceschelli, M., Elter, F. M., Puxeddu, M., & Utzeri, D. (2008). Petrogenesis of Al–silicate-bearing trondhjemitic migmatites from NE Sardinia, Italy. *Lithos*, *102*(3-4), 554–574.

D’lemos, R. S., Brown, M., & Strachan, R. A. (1992). Granite magma generation, ascent and emplacement within a transpressional orogen. *Journal of the Geological Society*, *149*(4), 487–490.

Daczko, N. R., & Piazolo, S. (2022). Recognition of melferite–A rock formed in syn-deformational high-strain melt-transfer zones through sub-solidus rocks: A review and synthesis of microstructural criteria. *Lithos*, 430–431, 106850.

Daczko, N. R., Piazolo, S., Meek, U., Stuart, C. A., & Elliott, V. (2016). Hornblendite delineates zones of mass transfer through the lower crust. *Scientific Reports*, *6*(1), 1-6.

Davidson, C., Hollister, L. S., & Schmid, S. M. (1992). Role of melt in the formation of a deep-crustal compressive shear zone: The MaClaren Glacier Metamorphic Belt, south central Alaska. *Tectonics*, *11*(2), 348–359.

Davidson, C., Schmid, S. M., & Hollister, L. S. (1994). Role of melt during deformation in the deep crust. *Terra Nova*, *6*(2), 133–142.

Didier, J. (1973). *Granites and their Enclaves: The Bearing of Enclaves on the Origin of Granites*. Developments in Petrology, 3. Elsevier.

Diener, J. F., White, R. W., & Hudson, T. J. (2014). Melt production, redistribution and accumulation in mid-crustal source rocks, with implications for crustal-scale melt transfer. *Lithos*, *200*, 212–225.

Druguet, E., & Carreras, J. (2006). Analogue modelling of syntectonic leucosomes in migmatitic schists. *Journal of Structural Geology*, *28*(10), 1734–1747.

Dyck, B., Waters, D. J., St-Onge, M. R., & Searle, M. P. (2020). Muscovite dehydration melting: Reaction mechanisms, microstructures, and implications for anatexis. *Journal of Metamorphic Geology*, *38*(1), 29–52.

Etheridge, M. A., Daczko, N. R., Chapman, T., & Stuart, C. A. (2020). Mechanisms of melt extraction during lower crustal partial melting. *Journal of Metamorphic Geology, 39*(1), 57–75.

Ghatak, H., Gardner, R. L., Daczko, N. R., Piazolo, S., & Milan, L. (2022). Oxide enrichment by syntectonic melt-rock interaction. *Lithos*, *414*, 106617.

Godinho, J. R., Piazolo, S., & Evans, L. (2014). Simulation of surface dynamics during dissolution as a function of the surface orientation: Implications for non-constant dissolution rates. *Earth and Planetary Science Letters*, *408*, 163–170.

Godinho, J. R., Putnis, C. V., & Piazolo, S. (2013). Direct observations of the dissolution of fluorite surfaces with different orientations. *Crystal Growth & Design*, *14*(1), 69–77.

Grandstaff, D. E. (1978). Changes in surface area and morphology and the mechanism of forsterite dissolution. *Geochimica et Cosmochimica Acta*, *42*(12), 1899–1901.

Green, T. H., & Watson, E. B. (1982). Crystallization of apatite in natural magmas under high pressure, hydrous conditions, with particular reference to 'orogenic' rock series. *Contributions to Mineralogy and Petrology*, *79*(1), 96–105.

Griffin, W. L. (2008). GLITTER: data reduction software for laser ablation ICP-MS. *Laser Ablation ICP-MS in the Earth Sciences: Current practices and outstanding issues*, 308–311.

Haines, P. W., Hand, M., & Sandiford, M. (2001). Palaeozoic synorogenic sedimentation in central and northern Australia: a review of distribution and timing with implications for the evolution of intracontinental orogens. *Australian Journal of Earth Sciences*, *48*(6), 911–928.

Hand, M., & Sandiford, M. (1999). Intraplate deformation in central Australia, the link between subsidence and fault reactivation. *Tectonophysics, 305*(1), 121–140.

Heinrich, K. F. J. (1966). X-ray absorption uncertainty. *The electron microprobe*, 296.

Henke, B. L. (1985). Lawrence Berkeley Laboratories, unpublished.

Henry, D. J., Guidotti, C. V., & Thomson, J. A. (2005). The Ti-saturation surface for low-to-medium pressure metapelitic biotites: Implications for geothermometry and Ti-substitution mechanisms. *American Mineralogist*, *90*(2-3), 316–328.

Henry, H. (2018) Mantle Pyroxenites: Deformation and Seismic Properties. (Doctoral dissertation). Macquarie University, Sydney, Australia.

Henry, H., Tilhac, R., Griffin, W. L., O'Reilly, S. Y., Satsukawa, T., Kaczmarek, M. A., & Ceuleneer, G. (2017). Deformation of mantle pyroxenites provides clues to geodynamic processes in subduction zones: case study of the Cabo Ortegal Complex, Spain. *Earth and Planetary Science Letters*, *472*, 174–185.

Hollister, L. S. & Crawford, M. L. (1986). Melt-enhanced deformation: a major tectonic process. *Geology, 14*(7), 558–561.

Holness, M. B., & Sawyer, E. W. (2008). On the pseudomorphing of melt-filled pores during the crystallization of migmatites. *Journal of Petrology*, *49*(7), 1343–1363.

Hövelmann, J., Putnis, A., Geisler, T., Schmidt, B. C., & Golla-Schindler, U. (2010). The replacement of plagioclase feldspars by albite: observations from hydrothermal experiments. *Contributions to Mineralogy and Petrology*, *159*(1), 43–59.

Hutton, D. H. (1988). Granite emplacement mechanisms and tectonic controls: Inferences from deformation studies. *Earth and Environmental Science Transactions of the Royal Society of Edinburgh*, *79*(2–3), 245–255.

Jarosewich, E., Nelen, J. A., & Norberg, J. A. (1980). Reference samples for electron microprobe analysis. *Geostandards Newsletter, 4*(1), 43–47.

Johnson, S. E. (1999). Porphyroblast microstructures: a review of current and future trends. *American Mineralogist*, *84*(11–12), 1711–1726.

Kisters, A. F. M., Ward, R. A., Anthonissen, C. J., & Vietze, M. E. (2009). Melt segregation and far-field melt transfer in the mid-crust. *Journal of the Geological Society*, *166*(5), 905–918.

Kriegsman, L. M. (2001). Partial melting, partial melt extraction and partial back reaction in anatectic migmatites. *Lithos*, *56*(1), 75–96.

Kruse, R., & Stünitz, H. (1999). Deformation mechanisms and phase distribution in mafic high-temperature mylonites from the Jotun Nappe, southern Norway. *Tectonophysics*, *303*(1-4), 223–249.

Labotka, T. C., Cole, D. R., Fayek, M., Riciputi, L. R., & Stadermann, F. J. (2004). Coupled cation and oxygen-isotope exchange between alkali feldspar and aqueous chloride solution. *American Mineralogist*, *89*(11–12), 1822–1825.

Larsen, R. B. (2002). The distribution of rare-earth elements in K-feldspar as an indicator of petrogenetic processes in granitic pegmatites: Examples from two pegmatite fields in southern Norway. *The Canadian Mineralogist*, *40*(1), 137–152.

Law, R. D. (1990). Crystallographic fabrics: a selective review of their applications to research in structural geology. *Geological Society, London, Special Publications*, *54*(1), 335–352.

Law, R. D., Mainprice, D., Casey, M., Lloyd, G. E., Knipe, R. J., Cook, B., & Thigpen, J. R. (2010). Moine thrust zone mylonites at the Stack of Glencoul: I–microstructures, strain and influence of recrystallization on quartz crystal fabric development. *Geological Society, London, Special Publications*, *335*(1), 543–577.

Lee, A. L., Torvela, T., Lloyd, G. E., & Walker, A. M. (2018). Melt organisation and strain partitioning in the lower crust. *Journal of Structural Geology*, *113*, 188–199.

Levine, J. S. F., Mosher, S., & Siddoway, C. S. (2013). Relationship between syndeformational partial melting and crustal-scale magmatism and tectonism across the Wet Mountains, central Colorado. *Lithosphere, 5*(5), 456–476.

Levine, J. S., Mosher, S., & Rahl, J. M. (2016). The role of subgrain boundaries in partial melting. *Journal of Structural Geology*, *89*, 181–196.

Lister, G. S., & Hobbs, B. E. (1980). The simulation of fabric development during plastic deformation and its application to quartzite: the influence of deformation history. *Journal of Structural Geology*, *2*(3), 355–370.

Lister, G. S., & Snoke, A. W. (1984). S-C mylonites. *Journal of Structural Geology*, *6*(6), 617–638.

London, D. (2005). Granitic pegmatites: an assessment of current concepts and directions for the future. *Lithos*, *80*(1–4), 281–303.

Maidment, D., Hand, M., & Williams, I. (2005). Tectonic cycles in the Strangways Metamorphic Complex, Arunta inlier, central Australia: Geochronological evidence for exhumation and basin formation between two high-grade metamorphic events. *Australian Journal of Earth Sciences, 52*(2), 205–215.

Mancktelow, N. S., & Pennacchioni, G. (2005). The control of precursor brittle fracture and fluid–rock interaction on the development of single and paired ductile shear zones. *Journal of Structural Geology*, *27*(4), 645–661.

Marchildon, N., & Brown, M. (2003). Spatial distribution of melt-bearing structures in anatectic rocks from southern Brittany, France: implications for melt transfer at grain-to orogen-scale. *Tectonophysics*, *364*(3–4), 215–235.

Mawby, J., Hand, M., & Foden, J. (1999). Sm-Nd evidence for high–grade ordovician metamorphism in the Arunta block, central Australia. *Journal of Metamorphic Geology, 17*(6), 653–668.

McDonough, W. F., & Sun, S. S. (1995). The composition of the Earth. *Chemical Geology*, *120*(3–4), 223–253.

Meek, U., Piazolo, S., & Daczko, N. R. (2019). The field and microstructural signatures of deformation-assisted melt transfer: Insights from magmatic arc lower crust, New Zealand. *Journal of Metamorphic Geology*, *37*(6), 795–821.

Menegon, L., Pennacchioni, G., Heilbronner, R., & Pittarello, L. (2008). Evolution of quartz microstructure and c-axis crystallographic preferred orientation within ductilely deformed granitoids (Arolla unit, Western Alps). *Journal of Structural Geology*, *30*(11), 1332–1347.

Menegon, L., Stünitz, H., Nasipuri, P., Heilbronner, R., & Svahnberg, H. (2013). Transition from fracturing to viscous flow in granulite facies perthitic feldspar (Lofoten, Norway). *Journal of Structural Geology*, *48*, 95–112.

Nabelek, P. I., Whittington, A. G., & Sirbescu, M. L. C. (2010). The role of H2O in rapid emplacement and crystallization of granite pegmatites: Resolving the paradox of large crystals in highly undercooled melts. *Contributions to Mineralogy and Petrology*, *160*(3), 313–325.

Passchier, C. W., & Trouw, R. A. (2005). *Microtectonics*. Springer Science & Business Media.

Passchier, C. W., Trouw, R. A. J., Zwart, H. J., & Vissers, R. L. M. (1992). Porphyroblast rotation: eppur si muove*?. *Journal of Metamorphic Geology*, *10*(3), 283–294.

Paterson, S. R., Fowler Jr., T. K., Schmidt, K. L., Yoshinobu, A. S., Yuan, E. S., & Miller, R. B. (1998). Interpreting magmatic fabric patterns in plutons. *Lithos 44*(1–2), 53–82.

Patiño Douce, A. E., & Johnston, A. D. (1991). Phase equilibria and melt productivity in the pelitic system: implications for the origin of peraluminous granitoids and aluminous granulites. *Contributions to Mineralogy and Petrology*, *107*(2), 202–218.

Piazolo, S., Daczko, N., Silva, D., & Raimondo, T. (2020). Melt-present shear zones enable intracontinental orogenesis. *Geology 48*(7), 643–648.

Raimondo, T., Clark, C., Hand, M., & Faure, K. (2011). Assessing the geochemical and tectonic impacts of fluid-rock interaction in mid-crustal shear zones: a case study from the intracontinental Alice Springs orogen, central Australia. *Journal of Metamorphic Geology, 29*(8), 821–850.

Raimondo, T., Hand, M., & Collins, W. J. (2014). Compressional intracontinental orogens: Ancient and modern perspectives. *Earth–Science Reviews, 130*, 128–153.

Rasband, W. S. (1997–2018). ImageJ, U. S. National Institutes of Health. Bethesda, MD, USA. Available at: http://imagej.nih.gov/ij/.

Ree, J. H., Kim, H. S., Han, R., & Jung, H. (2005). Grain-size reduction of feldspars by fracturing and neocrystallization in a low-grade granitic mylonite and its rheological effect. *Tectonophysics*, *407*(3–4), 227–237.

Rosenberg, C. L., & Handy, M. R. (2005). Experimental deformation of partially melted granite revisited: implications for the continental crust. *Journal of Metamorphic Geology*, *23*(1), 19–28.

Sawyer, E. W. (2008). *Atlas of migmatites* (Vol. 9). NRC Research press.

Scrimgeour, I. R. (2013). Developing a revised framework for the Arunta Region. In: Munson, T. J., Scrimgeour, I. R. (eds.), Annual Geoscience Exploration Seminar (AGES) Record of Abstracts. Northern Territory Geological Survey, Record 2003-001, Darwin, 1–8.

Searle, M. (2013). Crustal melting, ductile flow, and deformation in mountain belts: cause and effect relationships. *Lithosphere 5*(6), 547–554.

Shaw, R. D., Stewart, A. T., & Black, L. P. (1984). The Arunta Inlier: a complex ensialic mobile belt in central Australia. Part 2: tectonic history. *Australian Journal of Earth Sciences*, *31*(4), 457–484.

Silva, D., Daczko, N., Piazolo, S., Raimondo, T. (2022). Glimmerite: a product of melt-rock interaction within a crustal-scale high-strain zone. *Gondwana Research, 105*, 160–184.

Silva, D., Piazolo, S., Daczko, N. R., Houseman, G., Raimondo, T., & Evans, L. (2018). Intracontinental orogeny enhanced by far-field extension and local weak crust. *Tectonics*, *37*(12), 4421–4443.

Skemer, P., Katayama, I., Jiang, Z., & Karato, S. I. (2005). The misorientation index: Development of a new method for calculating the strength of lattice-preferred orientation. *Tectonophysics*, *411*(1–4), 157–167.

Stuart, C. A., Daczko, N. R., & Piazolo, S. (2017). Local partial melting of the lower crust triggered by hydration through melt–rock interaction: an example from Fiordland, New Zealand. *Journal of Metamorphic Geology, 35*(2), 213–230.

Stuart, C. A., Piazolo, S., & Daczko, N. R. (2018). The recognition of former melt flux through high-strain zones. *Journal of Metamorphic Geology*, *36*(8), 1049–1069.

Svahnberg, H., & Piazolo, S. (2010). The initiation of strain localisation in plagioclase-rich rocks: Insights from detailed microstructural analyses. *Journal of Structural Geology*, *32*(10), 1404–1416.

Ten Grotenhuis, S. M., Trouw, R. A. J., & Passchier, C. W. (2003). Evolution of mica fish in mylonitic rocks. *Tectonophysics*, *372*(1–2), 1–21.

Tetley, M. G., & Daczko, N. R. (2014). Virtual Petrographic Microscope: a multi-platform education and research software tool to analyse rock thin-sections. *Australian Journal of Earth Sciences*, *61*(4), 631–637.

Teyssier, C. (1985). A crustal thrust system in an intracratonic tectonic environment. *Journal of Structural Geology, 7*(6), 689–700.

Tullis, J., & Yund, R. A. (1985). Dynamic recrystallization of feldspar: a mechanism for ductile shear zone formation. *Geology*, *13*(4), 238–241.

Tullis, J., & Yund, R. A. (1991). Diffusion creep in feldspar aggregates: experimental evidence. *Journal of Structural Geology*, *13*(9), 987–1000.

Van der Molen, I., & Paterson, M. S. (1979). Experimental deformation of partially-melted granite. *Contributions to Mineralogy and Petrology*, *70*(3), 299–318.

Varga, J., Raimondo, T., Hand, M., Curtis, S., & Daczko, N. (2022). Hydration, melt production and rheological weakening within an intracontinental gneiss dome. *Lithos*, 432–433, 106872.

Vernon, R. H. (1986). K-feldspar megacrysts in granites—phenocrysts, not porphyroblasts. *Earth-Science Reviews*, *23*(1), 1–63.

Vernon, R. H. (1987). Growth and concentration of fibrous sillimanite related to heterogeneous deformation in K-feldspar-sillimanite metapelites. *Journal of Metamorphic Geology*, *5*(1), 51–68.

Vernon, R. H. (2000). Review of microstructural evidence of magmatic and solid-state flow. *Visual Geosciences*, *5*(2), 1–23.

Vernon, R. H. (2011). Microstructures of melt-bearing regional metamorphic rocks. *Geological Society of America Memoirs*, *207*, 1–11.

Vernon, R. H., & Paterson, S. R. (2008). How late are K-feldspar megacrysts in granites? *Lithos*, *104*(1–4), 327–336.

Vernon, R. H., Williams, V. A., & D'arcy, W. F. (1983). Grain-size reduction and foliation development in a deformed granitoid batholith. *Tectonophysics*, *92*(1–3), 123–145.

Vigneresse, J. L. (1995). Crustal regime of deformation and ascent of granitic magma. *Tectonophysics, 249*(3–4), 187–202.

Vigneresse, J. L., & Tikoff, B. (1999). Strain partitioning during partial melting and crystallizing felsic magmas. *Tectonophysics*, *312*(2–4), 117–132.

Von Bargen, N., & Waff, H. S. (1986). Permeabilities, interfacial areas and curvatures of partially molten systems: results of numerical computations of equilibrium microstructures. *Journal of Geophysical Research: Solid Earth*, *91*(B9), 9261–9276.

Weinberg, R. F. (1999). Mesoscale pervasive felsic magma migration: alternatives to dyking. *Lithos* *46*(3), 393–410.

Weinberg, R. F., Hasalová, P., Ward, L., & Fanning, C. M. (2013). Interaction between deformation and magma extraction in migmatites: Examples from Kangaroo Island. *South Australia Bulletin, 125*(7–8), 1282–1300.

Weinberg, R. F., Sial, A. N., & Mariano, G. (2004). Close spatial relationship between plutons and shear zones. *Geology*, *32*(5), 377–380.

Weinberg, R. F., Sial, A. N., & Pessoa, R. R., (2001). Magma flow within the Tavares pluton, northeastern Brazil: Compositional and thermal convection. *Geological Society of America Bulletin*, *113*(4), 508–520.

Whitney, D. L., & Evans, B. W. (2010). Abbreviations for names of rock-forming minerals. *American Mineralogist*, *95*(1), 185–187.

Wickham, S. M. (1987). The segregation and emplacement of granitic magmas. *Journal of the Geological Society*, *144*(2), 281–297.

Wilson, C. J. L. (1980). Shear zones in a pegmatite: a study of albite-mica-quartz deformation. *Journal of Structural Geology*, *2*(1–2), 203–209.

Winkler, H. G. F., & Schultes, H. (1982). On the problem of alkali feldspar phenocrysts in granitic-rocks. *Neues Jahrbuch fur Mineralogie Monatshefte*, *12*, 558–564.

Winter, J. D. (2013). *Principles of Igneous and Metamorphic Petrology*. Pearson education, London, UK.

Wolfram, L. C., Weinberg, R. F., Hasalová, P., & Becchio, R. (2017). How melt segregation affects granite chemistry: Migmatites from the Sierra de Quilmes, NW Argentina. *Journal of Petrology*, *58*(12), 2339–2364.

Yardley, B. W. (1977). The nature and significance of the mechanism of sillimanite growth in the Connemara Schists, Ireland. *Contributions to Mineralogy and Petrology*, *65*(1), 53–58.

Žák, J., Verner, K., & Týcová, P. (2008). Grain-scale processes in actively deforming magma mushes: New insights from electron backscatter diffraction (EBSD) analysis of biotite schlieren in the Jizera granite, Bohemian Massif. *Lithos*, *106*(3–4), 309–322.

Závada, P., Schulmann, K., Konopásek, J., Ulrich, S., & Lexa, O. (2007). Extreme ductility of feldspar aggregates—Melt-enhanced grain boundary sliding and creep failure: Rheological implications for felsic lower crust. *Journal of Geophysical Research: Solid Earth*, *112*(B10210), 1–15.

Zibra, I., Gessner, K., Smithies, H. R., & Peternell, M. (2014). On shearing, magmatism and regional deformation in Neoarchean granite-greenstone systems: Insights from the Yilgarn Craton. *Journal of Structural Geology*, *67*(B), 253–267.

FIGURE CAPTIONS

Fig. 1. Geological map of the SE Arunta Region showing study and sample locality (red star). The map emphasises the distribution of regional high-strain zones of hydrous schistose composition (e.g., Gough Dam shear zone, #1; yellow structures and respective number in map) in the mostly granulite and amphibolite facies rocks incorporating the Arunta Region. Represented are the regional anastomosing high-strain zones and thrust faults relative to the Strangways Metamorphic Complex (SMC) and the Harts Range Group (HRG). Simplified structural cross-sections (modified after Raimondo *et al.,* 2014) display the principal crustal discontinuities and high-strain zones of the main geological domains in the Arunta Region associated with the Alice Springs Orogeny (Collins & Teyssier, 1989; Ballèvre *et al.,* 2000; Maidment *et al.*, 2005; Raimondo *et al.,* 2011; Scrimgeour, 2013). #1 Gough Dam shear zone (GDSZ); #2 West Bore shear zone; #3 Wallaby Knob shear zone; #4 Yambah shear zone; #5 Southern Cross shear zone; #6 Harry Creek shear zone (HCSZ); #7 Erontonga/Two Mile Bore shear zone; #8 Illogwa shear zone; #9 Delny shear zone.

Fig. 2. Field relationships of the Gough Dam shear zone including sample localities. (a) Outcrop presenting biotite-rich glimmerite schist bands (white arrows) and trails of granitic lenses along the foliation (red arrows), both cutting a host of modified felsic granulite and granitic gneiss (S1: N102°/70°); (b) Outcrop of meter-scale glimmerite schist with a well-developed foliation (S1) that contains layers and lenses of partially modified relict felsic rock types. Field sense of shear is top to

the north (S1: N78°/70°); (c, d) Outcrop-scale and detailed views of domains of the GDSZ containing a high abundance of variably deformed granitic lenses and glimmerite bands cutting modified granitic gneiss along foliation. Granitic lenses present asymmetric envelopes or selvedges of glimmerite composition; (e, f) Magnification of glimmerite schist outcrop containing granitic lenses, along with isolated and clustered facetted K-feldspar grains aligned along the foliation in the biotite dominated matrix of the glimmerite schist; (g) Hand sample and detailed view of the collected glimmerite schist used for petrographic study containing isolated and clustered, facetted, mm- to cm-wide K-feldspar grains; (h) Quartzite mylonite layer hosted by glimmerite schist. Glimmerite shows a reaction replacement relationship that “invades” the quartzite mylonite fractures in multiple directions.

Fig. 3. Hand specimen and petrographic characteristics of granitic lenses. (a) Hand samples GD1620A (left) and GD1617 (right) of granitic lens in modified granitic gneiss without and with glimmerite selvedge, respectively. Coloured dashed lines shows contact of granitic lens with granitic gneiss; (b) Crossed-polarised photomicrograph of granitic lens and its contact with granitic gneiss in sample GD1620A. Evidence of elongated interstitial plagioclase in (c) and low dihedral angles in (d) (see Fig. 2a for field relationship); (e) Crossed-polarised photomicrograph of extremity of granitic lens bead in modified granitic gneiss featuring a glimmerite selvedge (sample GD1617). Quartz grain from modified granitic gneiss in glimmerite selvedge shows embayments filled with biotite and interstitial quartz, occasionally with low apparent dihedral angles between two biotite grains (see Fig. 2c, d for field relationship).

Fig. 4. Petrographic characteristics of glimmerite schist, sample GD1606. (a) Crossed-polarised light thin-section photomicrograph of glimmerite schist sample showing top to the left (reverse) shear-sense informed by sigmoidal shapes formed by biotite, muscovite, quartz and sillimanite grains around subangular K-feldspar and muscovite grains. Biotite-rich C’-type shear bands are observed. Photomicrographs for region (b) and (c) display dominant biotite glimmerite matrix showing

preferred orientation following C'-type shear band and S-plane, respectively; (d) Thin section μ-XRF mineral assemblage map; (e) SEM-BSE image of agglomeration of K-feldspar grains along the foliation. Dashed lines highlight biotite, muscovite, quartz and sillimanite grains warping around subangular K-feldspar grains. Embayments of biotite and muscovite in K-feldspar are highlighted by yellow arrows.

Fig. 5. Detailed microstructural characteristics of glimmerite schist, SEM-BSE and crossed-polarised light photomicrographs; sample GD1606. (a–d) Glimmerite schist sample presenting reaction replacement of (1) K-feldspar by biotite, muscovite and plagioclase "invasions" in embayments [panel a–c]; (2) low-pressure area between the trail of coarse K-feldspar grains presenting wrapping biotite band and interstitial quartz and trail of small K-feldspar grains [panel b]; and (3) coarse muscovite grain featuring a pressure shadow tail comprising biotite, quartz and minor K-feldspar grains [panel d]; (e, f) Crossed-polarised light photomicrographs of the featured region in panel (b) and (c) displaying the orientation and microstructures of the dominant biotite, quartz and muscovite present in the bands that warp around K-feldspar and located along the S-plane. Mineral abbreviations follow Whitney & Evans (2010).

Fig. 6. Mineral chemistry of K-feldspar core, rim and interstitial grains plotted on An-Ab-Or ternary diagram classification.

Fig. 7. K-feldspar grains chondrite-normalised REE patterns. (a) REE patterns for a diverse set of K-feldspar (isolated coarse grains and interstitial grains) in glimmerite schist and K-feldspar coarse grains in a granitic lens; (b) REE patterns plot from literature of non-GDSZ located K-feldspar present in pegmatite (Larsen, 2002), K-feldspar from leucocratic segregation in migmatites (Bea *et al.,* 1994; Carvalho *et al.,* 2016) and K-feldspar from the matrix of a granodiorite gneiss at granulite facies

(Bingen *et al.,* 1990); (c) REE patterns from K-feldspar rims (red lines) and interstitial grains (green lines; see Fig. 4e) possibly enriched in Eu compared to K-feldspar cores (black lines).

Fig. 8. Quantitative orientation analysis of K-feldspar and quartz; sample GD1606. (a) EBSD mineral phase map for quartz (red) and K-feldspar grains (blue) in glimmerite schist. Polymineralic sigmoidal shape and C'-type shear bands are indicated by the dashed white lines; (b) IPF-derived map for quartz grains relative to the X-plane; (c) Pole figures for all quartz grains and two groups of K-feldspar divided by grain size area, with a threshold at 0.5 per cent of map area, to distinguish coarse grains from interstitial grains. J- and M-index are displayed for all quartz grains and for interstitial K-feldspar grains. Uncorrelated misorientation angles distribution is featured for all grains from each mineral.

Fig. 9. Crystallographic misorientation map and embayments orientation of coarse K-feldspar grain. EBSD map comprised of band contrast and textural components showing the change in orientation within one coarse grain colour coded by crystallographic orientation divergence up to 5° relative to a reference orientation point. Coloured arrows highlight dissolution reaction sites on the K-feldspar grain and replacement by non-indexed minerals, i.e., mainly biotite and muscovite (top plane-polarised light photomicrograph), forming along the crystallographic axes of the K-feldspar grain. Quartz grains represented by variably grey EBSD band contrast, with rare sub-grain boundaries in yellow and common Dauphine twins in red. K-feldspar orientations of crystal faces are marked as coloured dashed lines.

Fig. 10. EBSD Euler and crystallographic misorientation maps of quartz and K-feldspar grains in glimmerite schist. (a) Interstitial low-strain area between two coarse K-feldspar grains presenting isolated quartz grains at a maximum misorientation of 15° relative to a reference point. Inset displays

Euler colours of K-feldspar grains showing two main orientation groups (pink versus green colours). Quartz grains are coloured red. Euler angle rotation is coloured as ψ - red, θ - green and φ – blue; (b) K-feldspar grain analysis for misorientation from a reference point up to 15° with each colour representing a different grain analysis. Embayments and their orientation are highlighted by the direction of the coloured arrows that match the coloured lines highlighting the orientation of relict K-feldspar grain facets shown in the pole figures for a, b and c crystallographic planes (equal area, lower hemisphere projection). The orientations of crystal faces are transferred to the EBSD map image as coloured dashed lines.

Fig. 11. Cartoon illustrating the proposed model of melt transfer zone collapse and subsequent entrapment of crystallised fraction from the externally derived migrating melt.

Table 1: Selected electron microprobe data on multiple minerals for glimmerite schist present in GDSZ.

Table 2: Representative REE composition of K-feldspar grains from GDSZ and non-GDSZ published data from multiple locations.

SUPPLEMENTARY MATERIAL

Fig. S1. Biotite in glimmerite schist Ti a.p.f.u. vs X_{Mg} a.p.f.u. graphical plot and Ti-in-biotite thermometry value estimation.

Table S1: Electron microprobe data of K-feldspar, plagioclase and biotite from glimmerite schist in the Gough Dam shear zone.

Table S2: LA-ICP-MS K-feldspar trace element data.

Fig. 1

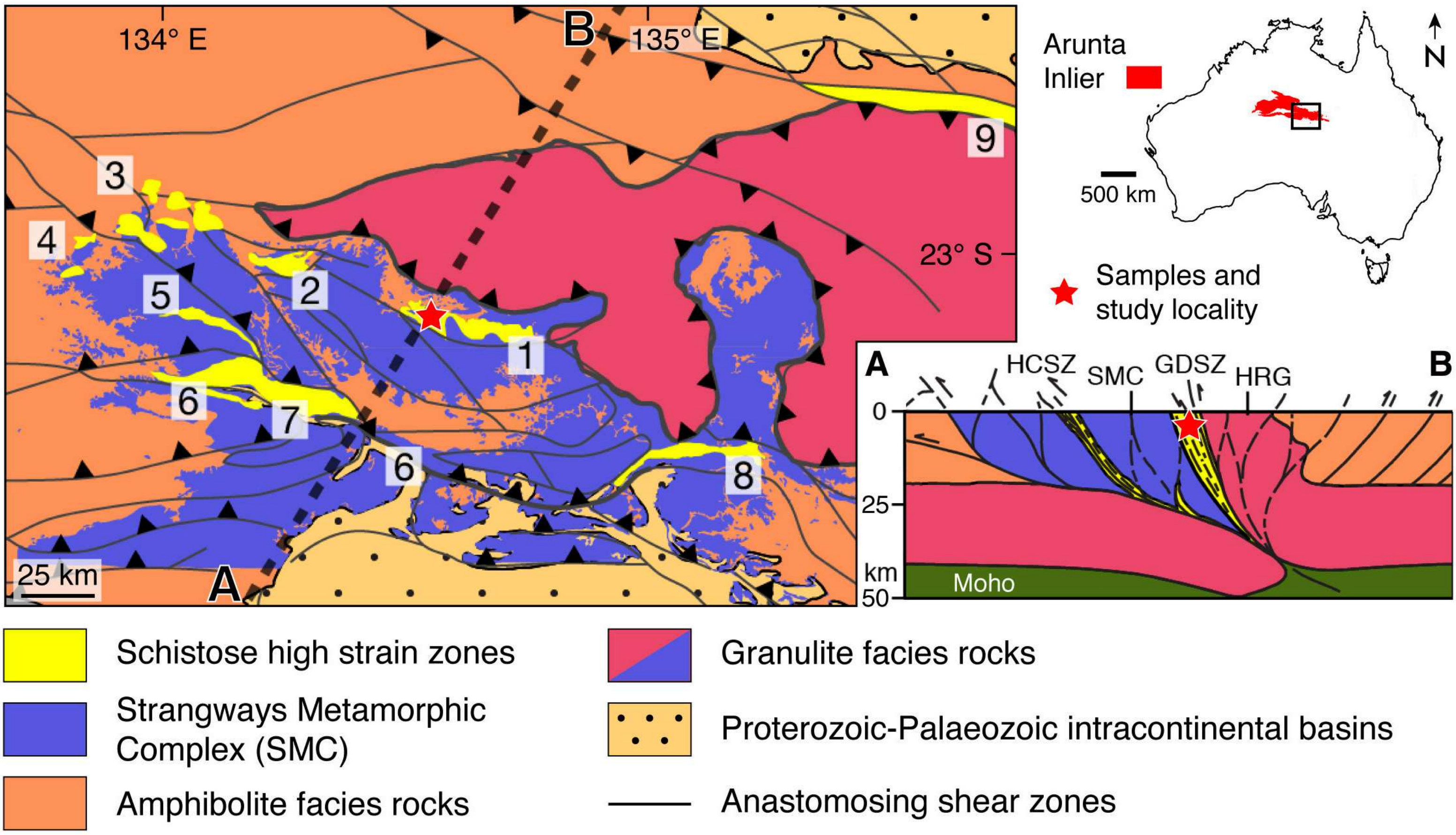

134° E
135° E
23° S
B
A
1
2
3
4
5
6
7
6
8
9
25 km
Arunta
Inlier
500 km
N
Samples and
study locality
A
B
HCSZ
SMC
GDSZ
HRG
0
25
km
50
Moho
Schistose high strain zones
Strangways Metamorphic Complex (SMC)
Amphibolite facies rocks
Granulite facies rocks
Proterozoic-Palaeozoic intracontinental basins
Anastomosing shear zones

Fig. 2

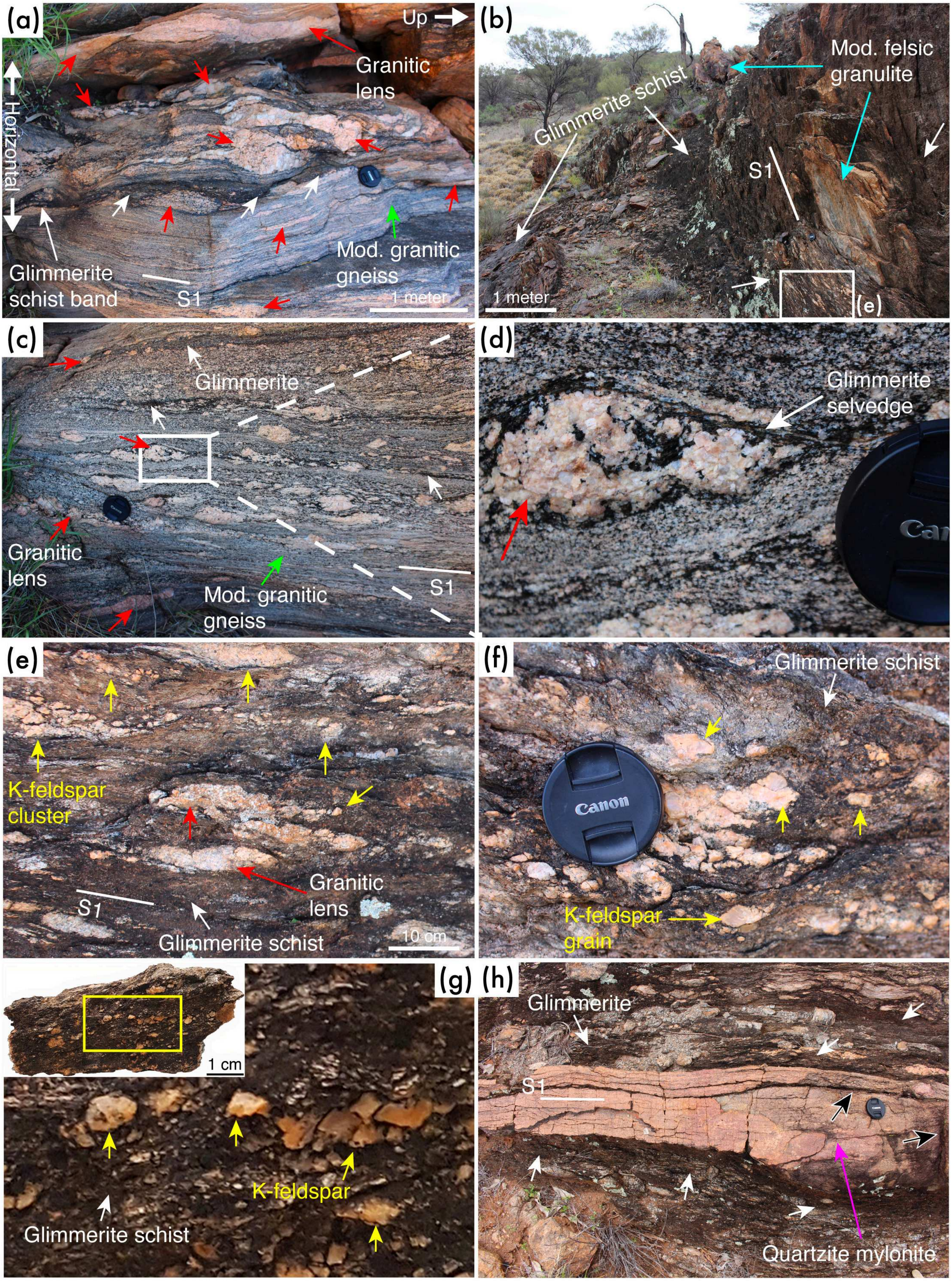

(a)
Up
Horizontal
Granitic lens
Glimmerite schist band
S1
Mod. granitic gneiss
1 meter
(b)
Glimmerite schist
Mod. felsic granulite
S1
1 meter
(e)
(c)
Glimmerite
Granitic lens
Mod. granitic gneiss
S1
(d)
Glimmerite selvedge
(e)
K-feldspar cluster
Granitic lens
S1
Glimmerite schist
10 cm
(f)
Glimmerite schist
K-feldspar grain
(g)
1 cm
K-feldspar
Glimmerite schist
(h)
Glimmerite
S1
Quartzite mylonite

Fig. 3

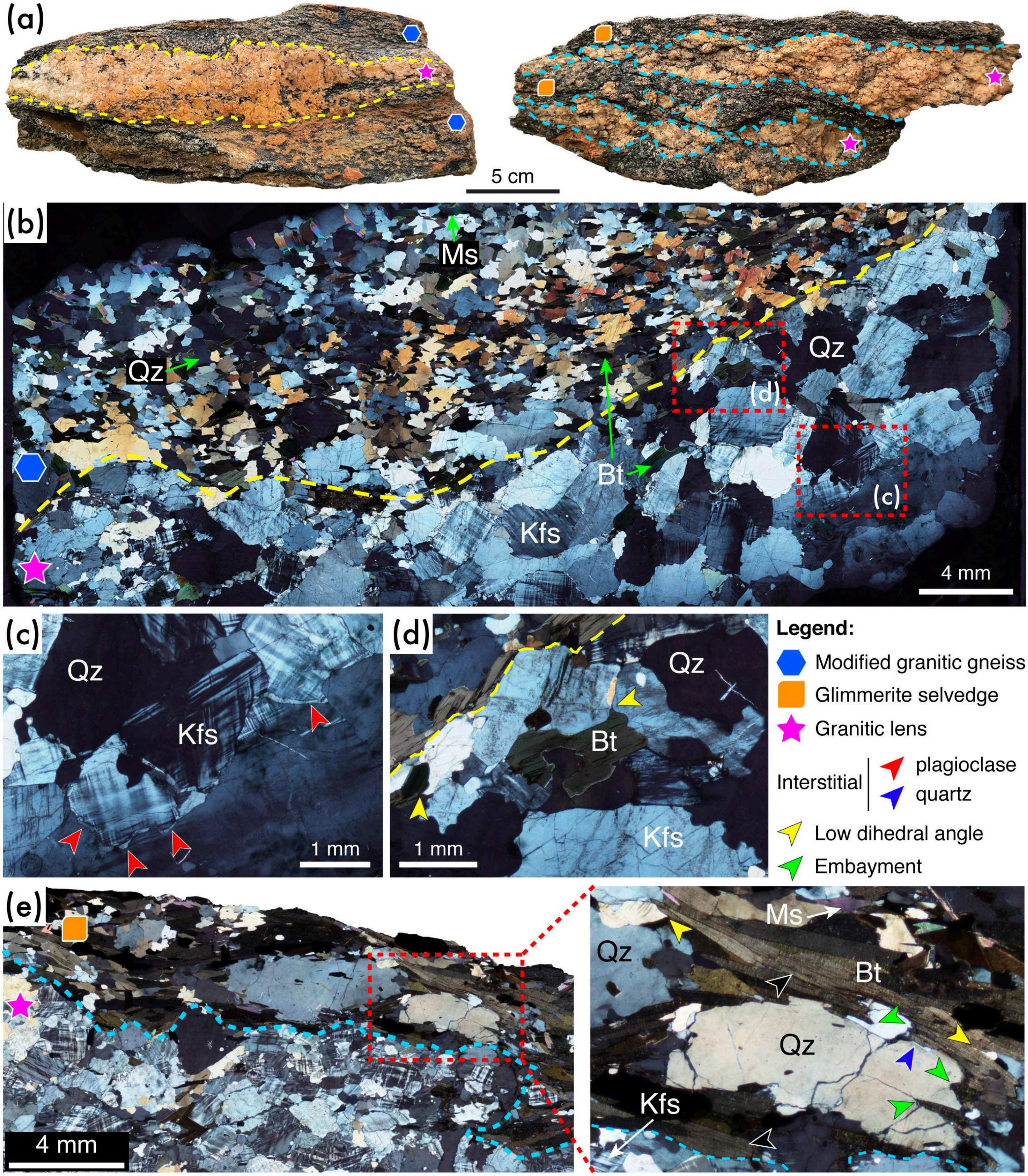

(a)
5 cm
(b)
Ms
Qz
Qz
(d)
Bt
Bt
(c)
Kfs
4 mm
(c)
Qz
Kfs
1 mm
(d)
Qz
Bt
Kfs
1 mm
Legend:
Modified granitic gneiss
Glimmerite selvedge
Granitic lens
Interstitial
plagioclase
quartz
Low dihedral angle
Embayment
(e)
4 mm
Ms
Qz
Bt
Qz
Kfs

Fig. 4

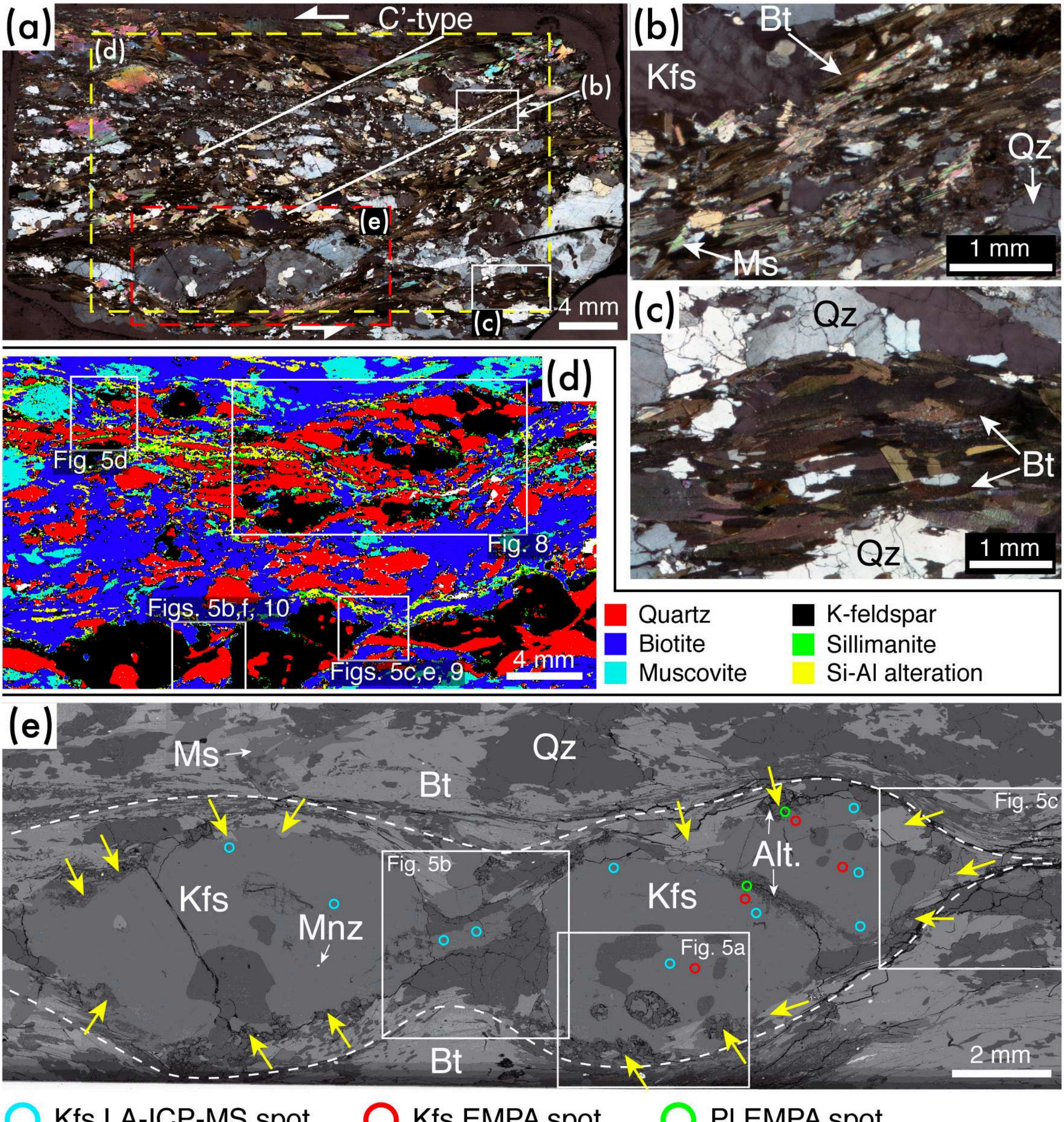

(a)
C'-type
(d)
(b)
(e)
(c)
4 mm
(b)
Bt
Kfs
Qz
Ms
1 mm
(c)
Qz
Bt
Qz
1 mm
(d)
Fig. 5d
Fig. 8
Figs. 5b,f, 10
Figs. 5c,e, 9
4 mm
Quartz
Biotite
Muscovite
K-feldspar
Sillimanite
Si-Al alteration
(e)
Ms
Qz
Bt
Alt.
Fig. 5c
Kfs
Mnz
Fig. 5b
Kfs
Fig. 5a
Bt
2 mm
Kfs LA-ICP-MS spot
Kfs EMPA spot
Pl EMPA spot

Fig. 5

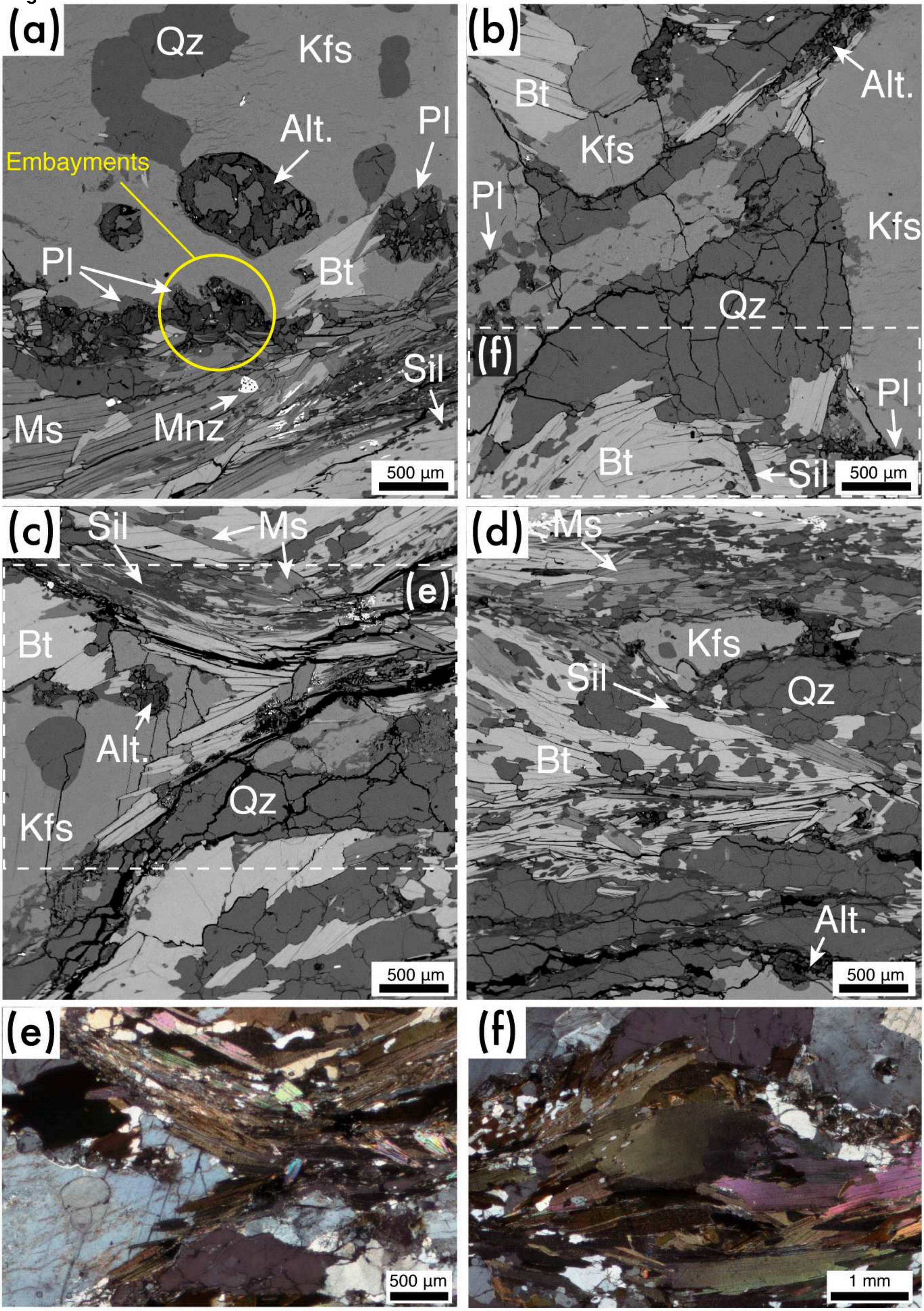

(a)
Qz
Kfs
Alt.
Pl
Embayments
Pl
Bt
Sil
Ms
Mnz
500 µm
(b)
Bt
Kfs
Alt.
Pl
Kfs
Qz
(f)
Pl
Bt
Sil
500 µm
(c)
Sil
Ms
(e)
Bt
Alt.
Qz
Kfs
500 µm
(d)
Ms
Kfs
Sil
Qz
Bt
Alt.
500 µm
(e)
500 µm
(f)
1 mm

Fig. 6

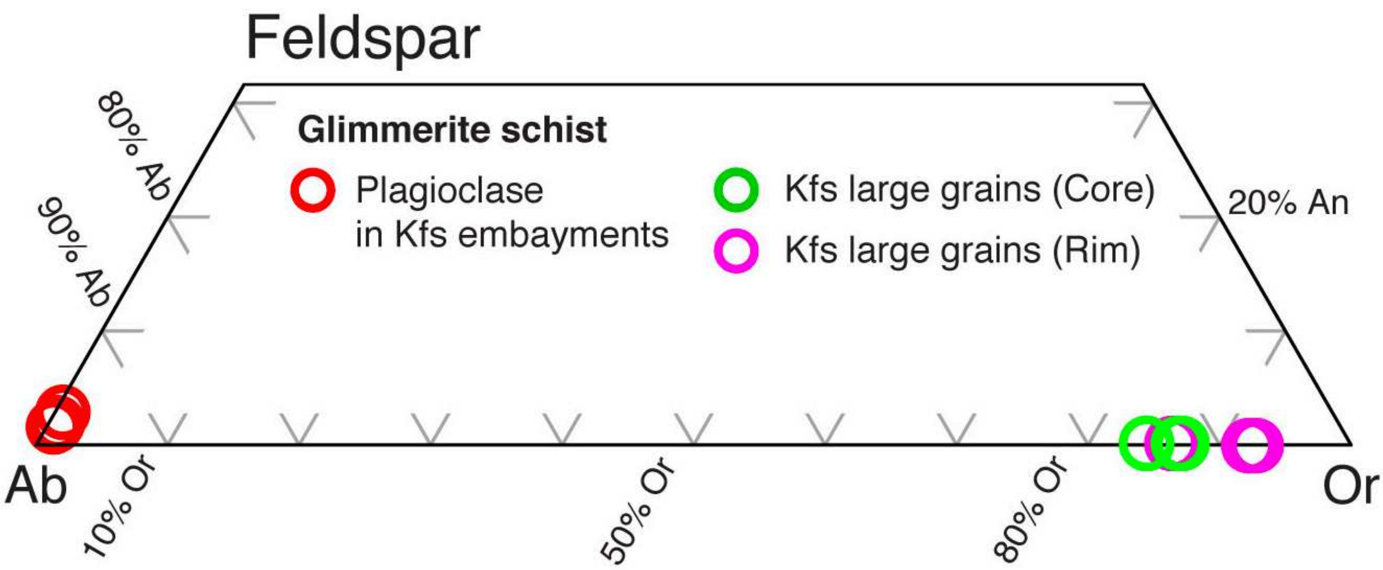
Feldspar
Glimmerite schist
Plagioclase
in Kfs embayments
Kfs large grains (Core)
Kfs large grains (Rim)
80% Ab
90% Ab
20% An
Ab
Or
10% Or
50% Or
80% Or

Fig. 7

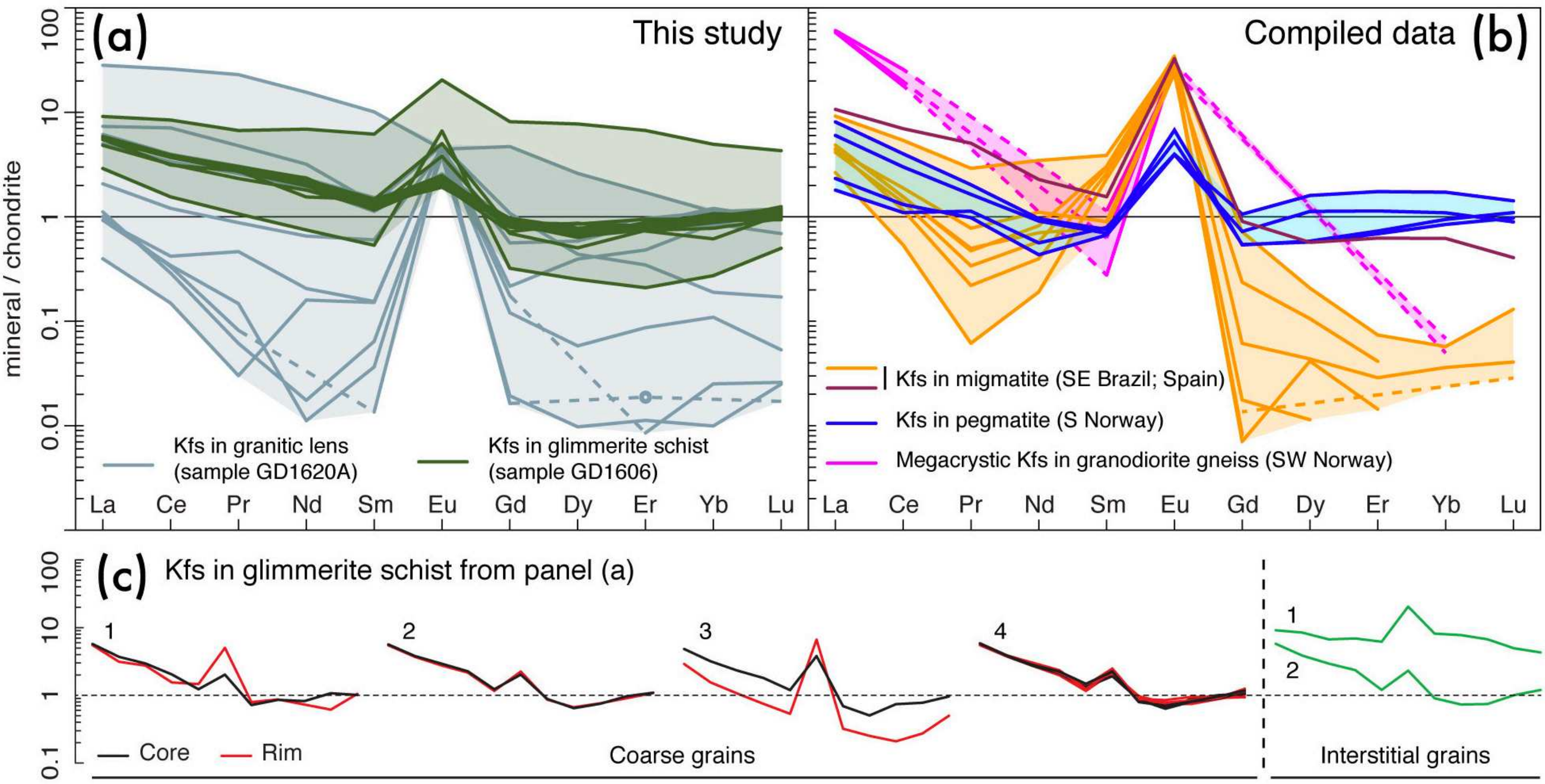

(a)
This study
mineral / chondrite
100
10
1
0.1
0.01
Kfs in granitic lens
(sample GD1620A)
Kfs in glimmerite schist
(sample GD1606)
La
Ce
Pr
Nd
Sm
Eu
Gd
Dy
Er
Yb
Lu
Compiled data
(b)
Kfs in migmatite (SE Brazil; Spain)
Kfs in pegmatite (S Norway)
Megacrystic Kfs in granodiorite gneiss (SW Norway)
(c)
Kfs in glimmerite schist from panel (a)
1
2
3
4
Core
Rim
Coarse grains
Interstitial grains

Fig . 8

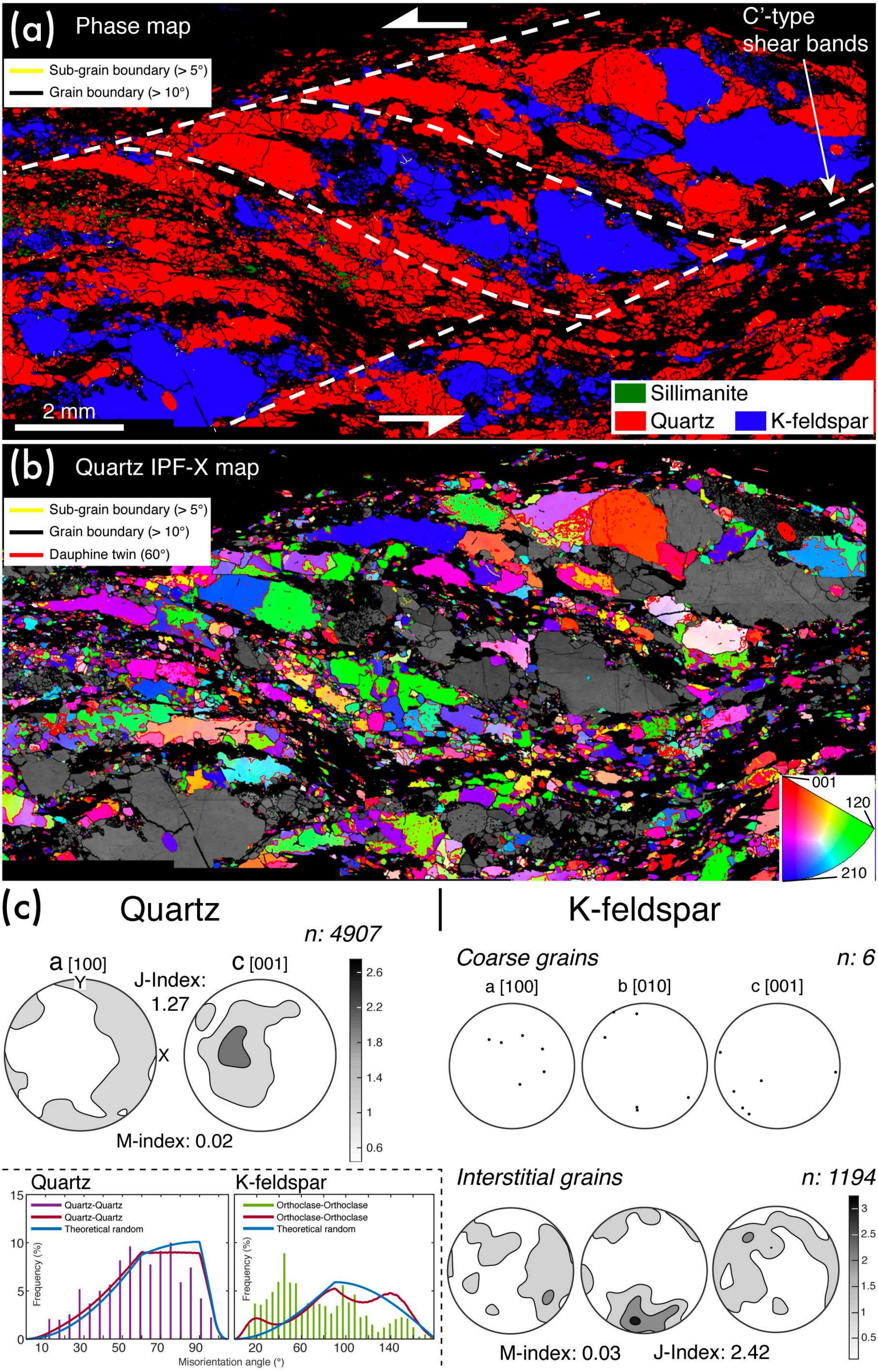

(a) Phase map
Sub-grain boundary (> 5°)
Grain boundary (> 10°)
C'-type shear bands
2 mm
Sillimanite
Quartz
K-feldspar
(b) Quartz IPF-X map
Sub-grain boundary (> 5°)
Grain boundary (> 10°)
Dauphine twin (60°)
001
120
210
(c)
Quartz
n: 4907
a [100]
Y
X
J-Index: 1.27
c [001]
M-index: 0.02
2.6
2.2
1.8
1.4
1
0.6
K-feldspar
Coarse grains
n: 6
a [100]
b [010]
c [001]
Interstitial grains
n: 1194
M-index: 0.03
J-Index: 2.42
3
2.5
2
1.5
1
0.5
Quartz
Quartz-Quartz
Quartz-Quartz
Theoretical random
K-feldspar
Orthoclase-Orthoclase
Orthoclase-Orthoclase
Theoretical random
Frequency (%)
Misorientation angle (°)

Fig. 9

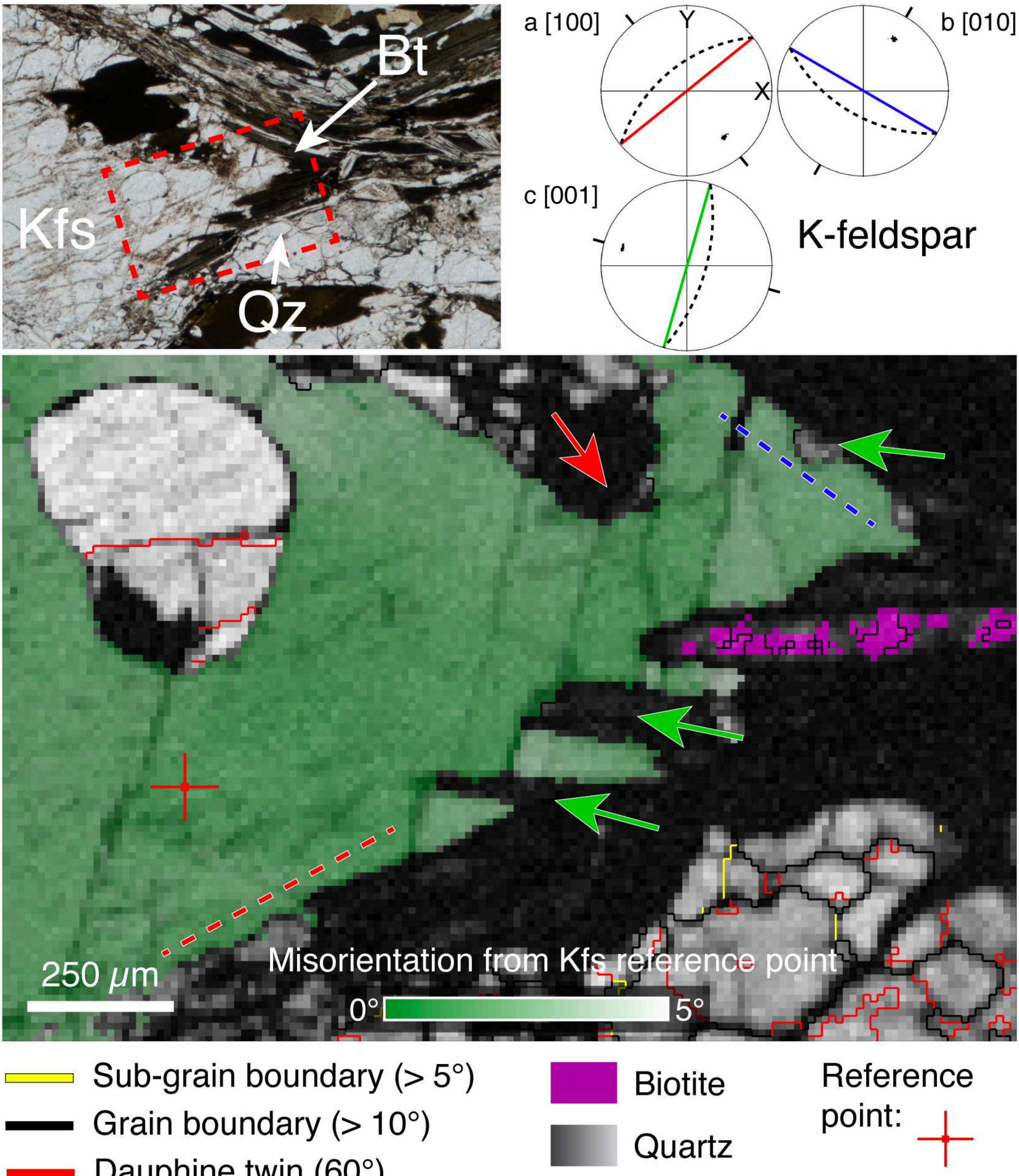
Bt
Kfs
Qz
a [100]
Y
X
b [010]
c [001]
K-feldspar
Misorientation from Kfs reference point
0°
5°
250 μm
Sub-grain boundary (> 5°)
Grain boundary (> 10°)
Dauphine twin (60°)
Biotite
Quartz
Reference point:

Fig. 10

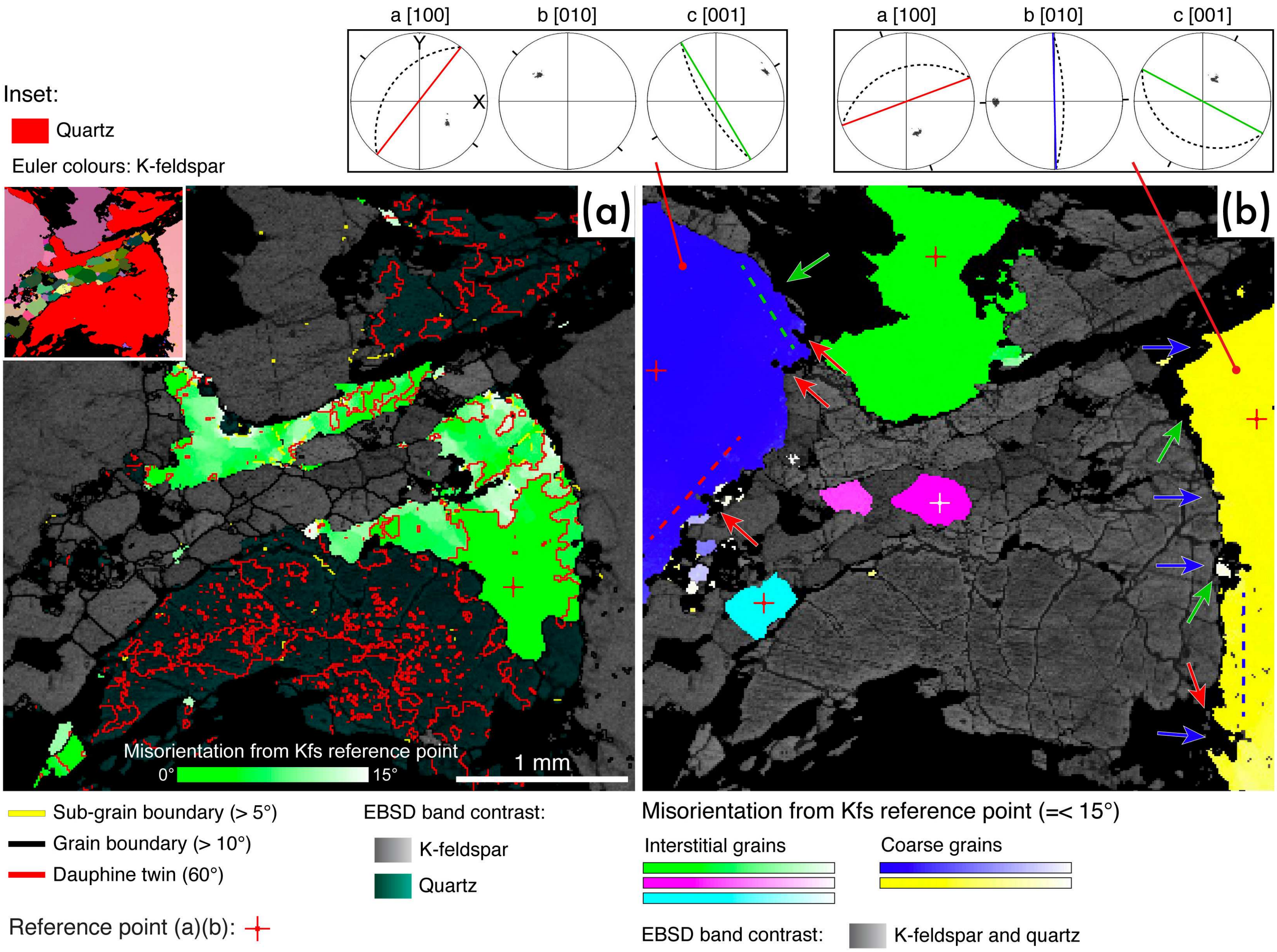
a [100]
b [010]
c [001]
Y
X
a [100]
b [010]
c [001]
Inset:
Quartz
Euler colours: K-feldspar
(a)
(b)
Misorientation from Kfs reference point
0°
15°
1 mm
Sub-grain boundary (> 5°)
Grain boundary (> 10°)
Dauphine twin (60°)
EBSD band contrast:
K-feldspar
Quartz
Reference point (a)(b):
Misorientation from Kfs reference point (=< 15°)
Interstitial grains
Coarse grains
EBSD band contrast:
K-feldspar and quartz

Fig. 11

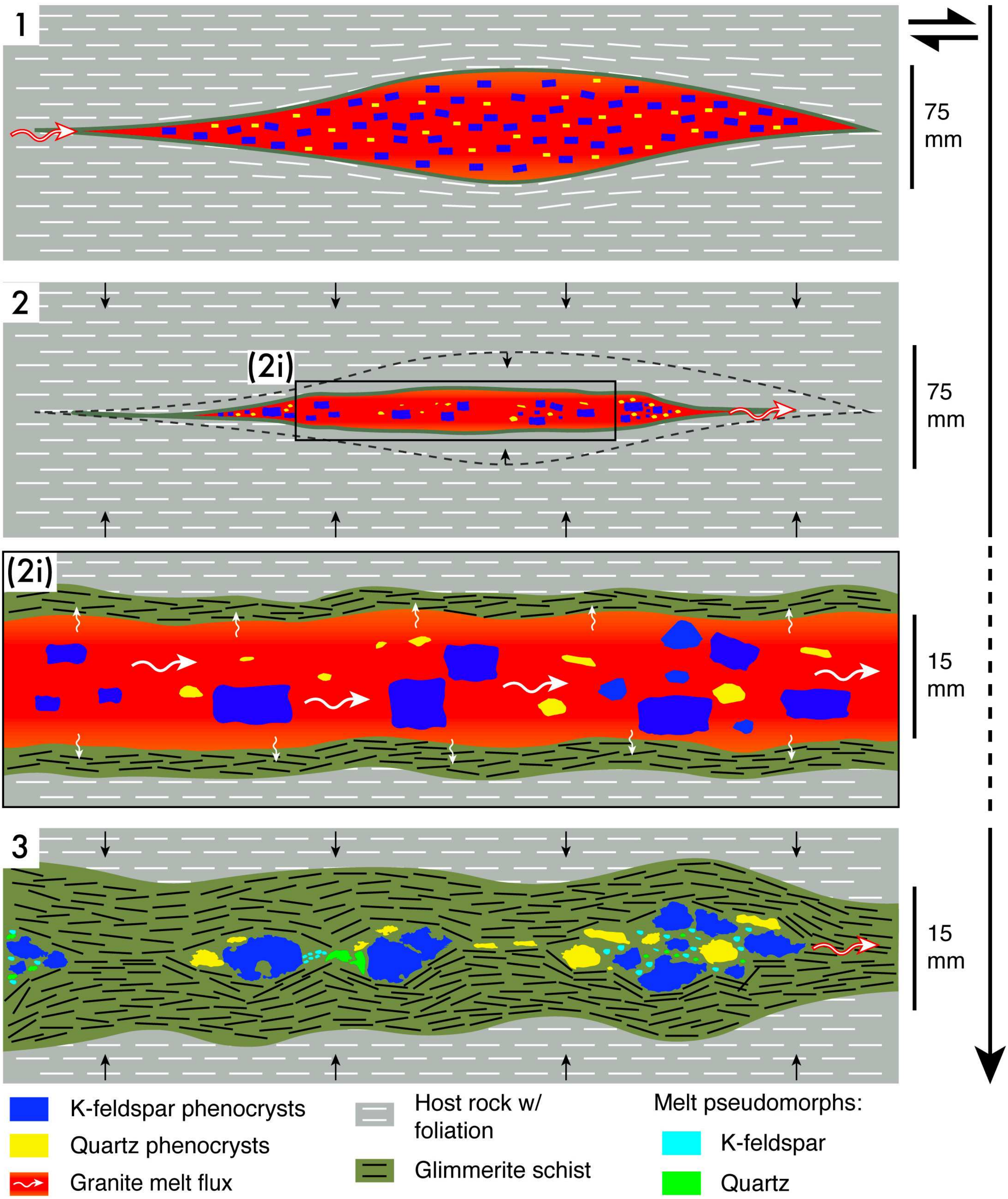

1
75
mm
2
(2i)
75
mm
(2i)
15
mm
3
15
mm
Time
K-feldspar phenocrysts
Quartz phenocrysts
Granite melt flux
Host rock w/
foliation
Glimmerite schist
Melt pseudomorphs:
K-feldspar
Quartz

Table 1: Selected electron microprobe data on multiple minerals for glimmerite schist present in GDSZ.

Sample	**Glimmerite schist (GD1606)**		
Mineral	*Bt*	*Kfs*	*Pl*
SiO_2 wt%	35.73	63.75	67.10
TiO_2	2.55	–	–
Al2O3	17.78	18.78	20.36
V_2O_3	0.04	–	–
Cr_2O_3	–	–	–
FeO_{total}	17.69	0.04	–
NiO	–	–	–
MnO	0.10	–	–
MgO	11.58	–	–
CaO	–	–	0.62
Na_2O	0.20	1.46	11.43
K_2O	9.71	14.18	0.11
P_2O_5	–	0.14	0.13
SO_3	–	–	–
Cl	0.41	0.04	–
F	0.59	–	–
O	-0.34	0.01	0.00
H_2O	3.93	0.00	0.00
Total	*99.97*	*98.41*	*99.73*

Mineral abbreviation follow Whitney & Evans (2010). (–): Below detection limit. The complete dataset is available in Table S1.

Table 2: Representative REE composition of K-feldspar grains from GDSZ and non-GDSZ published data from multiple locations.

	Gough Dam shear zone			**Compilation of published Kfs composition (non-GDSZ)**			
Sample/ *Mineral*	Glimmerite schist (GD1606)		Granitic lens (GD1620A)	Gneiss[1]	Pegmatite[2]	Migmatite[3][4]	
	Coarse grains	*Interstitial*					
La	5.755	9.139	2.072	60.759	6.013	10.684	4.869
Ce	3.830	8.450	1.206	25.775	3.002	6.982	1.558
Pr	2.963	6.703	0.879	- -	1.638	5.065	0.472
Nd	2.103	6.915	0.654	–	0.910	2.276	0.821
Sm	1.358	6.189	0.601	1.142	0.696	1.554	3.027
Eu	2.284	20.462	4.352	24.156	6.767	32.682	34.547
Gd	0.829	8.146	0.563	- -	0.538	0.905	0.061
Dy	0.663	7.748	0.585	- -	0.585	0.569	0.043
Er	0.885	6.713	0.869	- -	0.731	0.625	0.029
Yb	1.006	4.950	1.205	0.068	0.944	0.621	0.036
Lu	1.053	4.297	0.951	- -	1.098	0.407	0.041

REE values were normalised using McDonough & Sun (1995) chondritic values. (1) Granodiorite gneiss porphyroblasts (Bingen *et al.*, 1990); (2) Pegmatite (Larsen, 2002); (3) Peraluminous migmatite leucosome (Bea *et al.*, 1994); (4) Kfs-rich evolved leucosome (Carvalho *et al.*, 2016). Mineral abbreviation follow Whitney & Evans (2010). The complete dataset is available in Table S2. (–): Below detection limit; (- -): Not available.